Spring 2014

Evaluation of Mixing-Limited Quasi-Global Wind-US Model for HIFiRE 2 Flowpath

Michael R. Borghi Jr.
Embry-Riddle Aeronautical University - Daytona Beach

Evaluation of Mixing-Limited Quasi-Global Wind-US Model for HIFiRE 2 Flowpath

By

Michael R. Borghi Jr.

A Graduate Thesis Submitted to the

Department of Aerospace Engineering

In Partial Fulfilment of the Requirements for the Degree of

Masters of Science in Aerospace Engineering

Embry-Riddle Aeronautical University

Daytona Beach, FL

Spring 2014

Evaluation of Mixing-Limited Quasi-Global Wind-US Model for HIFiRE 2 Flowpath

By

Michael R. Borghi Jr

This thesis was prepared under the direction of the candidate's thesis committee chairman, Dr. William A. Engblom, Professor of Mechanical and Aerospace Engineering, and has been approved by the members of his thesis committee. It was submitted to the Aerospace engineering department and was accepted in partial fulfillment of the requirements for the degree of Masters of Science in Aerospace Engineering.

THESIS COMMITTEE

Dr. William A. Engblom, Chairman
Professor of Aerospace and Mechanical Engineering, Embry-Riddle Aeronautical University

Dr. Eric Perrell, Co-Chairman
Professor of Aerospace Engineering, Embry-Riddle Aeronautical University

Dr. Reda Mankbadi, Member
Professor of Aerospace Engineering, Embry-Riddle Aeronautical University

Dr. Yi Zhao, Graduate Program Coordinator
Aerospace Engineering, Embry-Riddle Aeronautical University

Dr. Robert Oxley
Associate Vice President for Academics, Embry-Riddle Aeronautical University

9-26-2014
Date

Acknowledgments

I would like to thank my loving wife, Nisa, who has supported me through my quest for higher education, and my parents who always encouraged me to follow my dreams. I also thank my advisor and friend, Dr. Bill Engblom for the continued support, guidance, and encouragement over the years I have worked with him.

I also thank Dr. Nick Georgidas from NASA Glenn, for providing the computational resources required, as well as lending his expertise to ensure the quality of this work. I would also like to thank Dr. Mankbadi, and Dr. Perrell for their continued advisement and participation on my thesis committee. I would also like to thank Michael Bynum of AMA, Inc., at NASA Langley for providing the experimental data and technical support.

The author would like to thank the NASA Advanced Supercomputing Division for providing the necessary computational resources, and to the College of Engineering at Embry-Riddle Aeronautical University for providing partial funding for this effort.

Table of Contents

Table of Figures

List of Tables

Abstract

Author: Michael R. Borghi Jr.

Title: Evaluation of Mixing-Limited Quasi-Global Wind-US Model for HIFire 2 Flowpath

Institution: Embry-Riddle Aeronautical University

Year: 2014

A Reynolds-averaged Navier-Stokes computational model featuring a mixing-limited, quasi-global chemical kinetics approach for an ethylene-methane fuel mixture is described and used in a validation effort against the Hypersonic International Flight Research Experimentation (HIFiRE) Direct Connect Rig experimental data for flight Mach numbers of 5.84, 6.5, and 8.0. An average error level between the numerical predictions and corresponding experimental measurements for static pressure along the engine flowpath is found to be within approximately 10%, for the two lowest Mach number cases, without calibration. Key features of the numerical flowfield development are identified, including regions within the combustor found to be significantly mixing-limited for each fuel type. The sensitivity of the results to turbulent Schmidt is also briefly examined.

I. Introduction

The Hypersonic International Flight Research Experimentation (HIFiRE) program is a collaborative international partnership between The U.S. Air Force Research Laboratory (AFRL) and the Australian Defense Science and Technology Origination (DTSO). The goals of HIFiRE are to:

1. study fundamental hypersonic flows through flight experimentation,
2. develop computational tools that accurately model the results of the flight experiments,
3. use those computational models to develop technologies required for the advancement to the next generation of high speed flight vehicles.

The HIFiRE program is composed of 8 separate experiments, each of which examines specific hypersonic phenomena. Each experiment will also be used to help grow verification tools such as numerical analyses, and ground tests [1]. Each of the 8 experiments will have been designed to include a final flight.

The second flight experiment (HF2) of the HIFiRE program took place in May 2012. It was a flight powered by booster rockets, to allow the desired flight conditions to be achieved without the added complexities of a full flight system. The HF2 flight primary objective was to evaluate a scramjet engine's performance through a mode transition from dual-mode operation at roughly Mach 5.5 to scram-mode operation at Mach 8+. Secondary objectives included providing a test bed for, and collecting higher fidelity measurements of performance parameters such as measuring combustion products.

As a part of the second flight (HF2), ground tests [2] were performed at NASA Langley's Arc-Heated Scramjet Test Facility (AHSTF). The AHSTF is located in Hampton Virginia, and facilities include a 20 MW power supply powering a Hules type arc-heater. The AHSTF operates by overheating a small (much less than stoichiometric) amount of air, and then mixing the heated air with 3 times the amount of unheated air achieving up to 2.27 kg/s mass flow. The AHSTF has been in operation since 1976 and has been used in excess of 1700 scramjet tests. The

Figure 1. HIFiRE II Flight Vehicle on Launch Pad

ground tests conducted in the AHSTF as part of HF2 are known as the HIFiRE Direct Connect Rig experiments (HDCR). A range of flight Mach numbers have been studied from Mach 5.5 to Mach 8.5 [1]

Recent attempts to use a RANS-based approach to simulate the HDCR experiments have proven effective, provided turbulence modeling is calibrated. Storch et al [3] were able to closely calibrate to HDCR experimental data by varying the turbulent Schmidt number, toggling a compressibility correction, and varying a relatively simple mixed-limited combustion model with VULCAN (they changed the EDC constant in their work) and a detailed laminar chemical kinetics approach with CFD++. Georgiadis et al [4] have recently conducted parametric studies of turbulence modeling and turbulent Schmidt number effects using a simplified kinetics approach with Wind-US.

The goal of this paper is to document the validation of the Wind-US flow solver with a more complete chemical kinetics approach, against the HDCR experimental data for flight Mach numbers of 5.84, 6.5, and 8.0. A mixing-limited, quasi-global chemical kinetics approach has been chosen, to be described below.

II. Numerical Methodology

A. Numerical Approach

Numerical simulations are conducted with the Wind-US flow CFD solver. Wind-US is developed by the NPARC Alliance, a partnership between NASA Glenn Research Center, USAF Arnold Engineering and Development Complex (AEDC), and Boeing Phantom Works [5]. It has been successfully applied to other direct-connect scramjet flow paths with both clean and vitiated supply air [6-8]. Recent development of Wind-US for high-speed flows include Damkohler-limited and mixing-limited combustion models, transition and turbulence models for compressible flow, and a conjugate heat transfer capability. More details regarding recent Wind-US development are found in [9].

B. Grid Definitions

The HDCR flowpath is illustrated in Figure 2. Surface definition of the HFDCRThe red region is the facility nozzle, the gray region is the engine flowpath, and the blue regions are the fuel injectors. On each of the body and cowl sides of the flowpath, there are 8 fuel injectors, 4 upstream of the cavity referred to as the *primary* injectors, and 4 downstream of the cavity referred to as *secondary* injectors. The primary and secondary injectors have diameters of 0.125" and 0.094", respectively. The primary injectors are angled 15º towards the core flow. The secondary injectors are normal to the flowpath walls. The AHSTF has 3 facility nozzles available, two nozzles were utilized to cover the entire Mach range of the HDCR tests [3]. The Mach 2.51 facility nozzle is used to simulate the isolator entrance state for the flight Mach numbers of 5.84 and 6.5. The Mach 3.46 nozzle provides for the flight Mach number of 8.0. Both facility nozzles were used in the following simulations.

A multi-block structured grid of 6.5 million cells has been created for the flowpath and were derived from the computational grids used in Storch et al [3]. A wall-integration approach is used, with y+ values of typically less than 5 along all wall surfaces. This is thought to be more appropriate for resolving shock-boundary layer interactions in the isolator than other methods, such as wall functions. Grids were constructed in a manner to permit sequencing from coarse to medium to fine levels. The block cell size is doubled in all three computational space directions when transitioning from coarse to medium level, or from medium to fine level. Two grids were used, differing only by the two different facility nozzles. The lower-speed computational mesh is displayed in Figure 3. Surface mesh for Wind-US flow simulation of HFDCR One quarter of the test facility is modeled based on symmetry considerations, and assumption of steady-state flow. The X-Y and X-Z planes are the symmetry planes about which the full flowpath is sliced to make the quarter grid. Thus, the computational mesh has two primary and two secondary injectors.

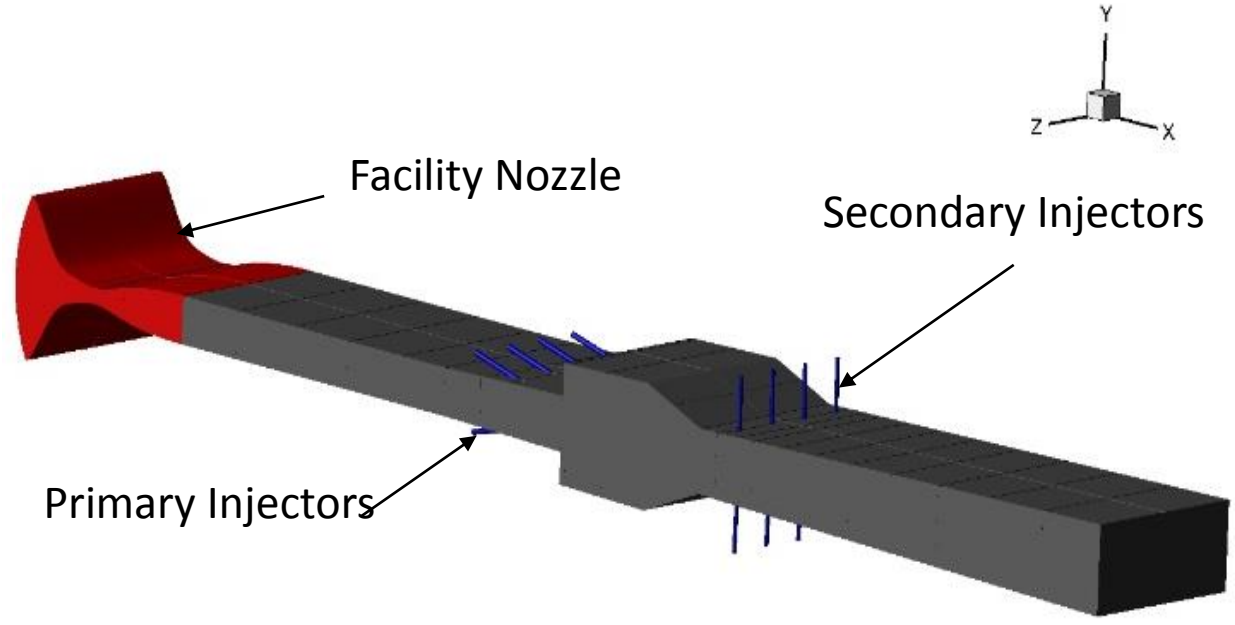

Figure 2. Surface definition of the HFDCR

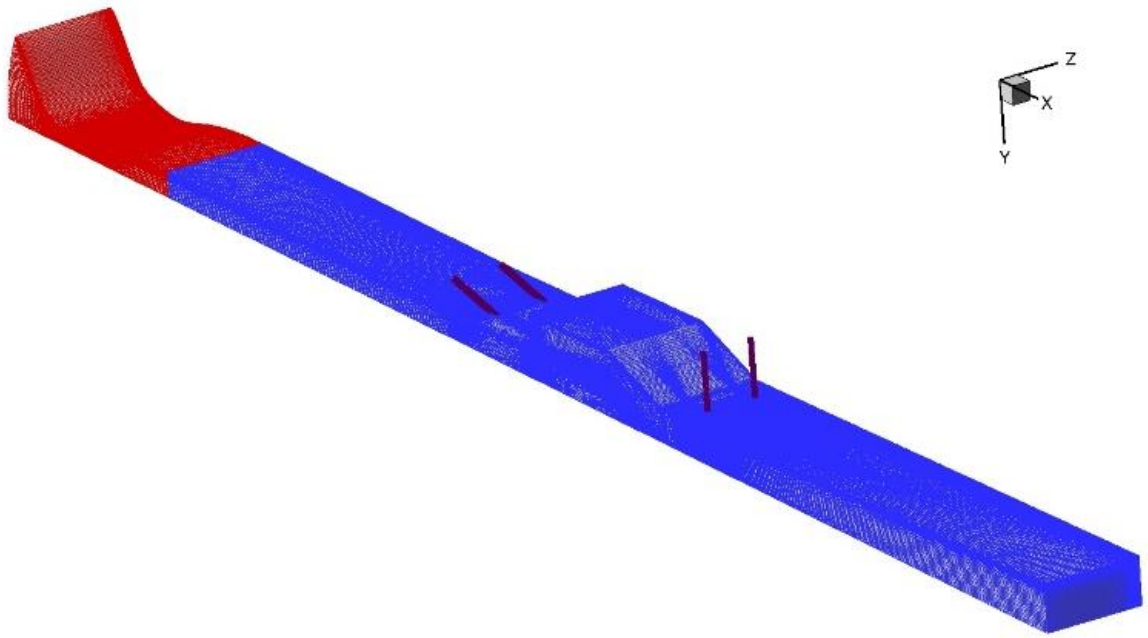

Figure 3. Surface mesh for Wind-US flow simulation of HFDCR

C. Numerical Matrix and Procedure

The computations completed for this paper corresponded to simulated flight Mach numbers of 5.84, 6.5, and 8.0 with clean air supply (i.e., not vitiated). Table 1 provides the conditions used for these simulation. Simulations at turbulent Schmidt numbers of 0.6 and 0.7 were completed for each of the three flight Mach numbers. Tare (no fuel) cases are also presented herein. All simulation results are compared for sake of validation against HDCR data from Storch et al [3]. The fuel is the composition of 36% CH_4 and 64% C_2H_4 by mole, in all cases.

Table 1. Wind-US Run Matrix

Case #	Experimental Run (# @ Time)	Simulated Flight Mach Number	Total Temp. (^{O}R)	Total Pressure (psia)	ϕ_{Total}	$\phi_{Primary}$	$\phi_{Secondary}$	Sc_t
1	123.1@7.5s	5.84	2790	215	0.65	0.15	0.50	0.6
2	125.1@12.0s	6.5	3326	217	1.0	0.4	0.6	0.6
3	136.3@18.0s	8.0	4625	620	1.0	0.4	0.6	0.6

4	123.1@7.5s	5.84	2790	215	0.65	0.15	0.50	0.7
5	125.1@12.0s	6.5	3326	217	1.0	0.4	0.6	0.7
6	136.3@18.0s	8.0	4625	620	1.0	0.4	0.6	0.7
1T	TARE	5.84	2790	215	0.0	0.0	0.0	0.6
2T	TARE	6.5	3326	217	0.0	0.0	0.0	0.6
3T	TARE	8.0	4625	620	0.0	0.0	0.0	0.6

Using the grid sequencing feature of Wind-US, medium and fine grid results are continued from the converged solutions from coarse and medium grid levels, respectively. Wind-US *Spawn* commands were used to execute scripts that were used to gather data to monitor convergence, including key combustion products at the nozzle exit, and axial pressure profiles. Sustained combustion was obtained and maintained in all reacting flow simulations without need for numerical "ignition," as found necessary in a previous effort [7].

III. Physical Models and Boundary Conditions

The Wind-US physical models applied in this study are similar to the models used in previous studies of variations on the Hy-V scramjet flowpath [6-8]. These previous models demonstrated a large degree of success in predicting the primary features of the axial pressure distribution along the internal flowpath, including mode transition. These models are briefly described below.

- Menter's shear stress transport (SST) turbulence model [10] with modified a_1 limiter per the recent work by Georgiadis [11].
- Gordon and McBride thermodynamic properties from the NASA Chemical Equilibrium and Applications (CEA) database is the source of all thermodynamics data.

- HLLC inviscid flux function [12] with 2nd-order upwind and TVD enforcement.
- Turbulent Prandtl and Schmidt of 0.89 and 0.6, respectively. The Schmidt number typically has a strong influence on high-speed combustion performance [3, 4, 6]. A limited sensitivity study on the effect of turbulent Schmidt is provided later in this paper.
- Damkohler number, based on the ratio of chemical and fluid dynamic time scales, is used to limit chemical reaction rates using an approach described by Eppard [13]. All converged results are obtained using a maximum Da of 100. Preliminary testing showed this limit to have a negligible effect on the converged solution.
- Hot isothermal wall temperature of 900°R and 1440°R are chosen for the supply nozzle walls and flowpath walls, respectively, based on examination of available thermocouple data. Preliminary testing showed the converged solution to be weakly sensitive to the flowpath wall temperature.

A detailed chemical kinetics mechanism, such as the H_2-O_2 mechanism used in these previous models, was not deemed practical for HIFiRE fuel combination of C_2H_4 and CH_4 due to the much larger number of species and reactions required. Additionally, researchers [3, 14] have demonstrated reasonable success in predicting high-speed hydrocarbon-fueled combustor performance when using the Eddy Dissipation Concept (EDC) to account for turbulence-chemistry interaction via mixing-limited reaction rates, as proposed by Magnussen [15]. Finally, it was desirable to build a model which would have sufficient detail to potentially be used to evaluate vitiation effects in future studies.

We chose to combine a "quasi-global" laminar chemical kinetics approach from Westbrook and Dryer [16] with an EDC treatment. The complete kinetic set is provided in Table 2, along

with implementation notes. The Westbrook and Dryer model includes a single-step, forward-only reaction to account for the oxidation of a hydrocarbon fuel into intermediate products of CO and H_2. An additional 21 reactions account for the CO-O_2-H_2 combustion system at a modest level of detail. Since the HIFiRE fuel consists of C_2H_4 and CH_4, two single-step forward reactions, were employed. The resulting laminar kinetics set includes 13 species and 23 reactions. However, 2 species (HO_2 and H_2O_2) and the related 10 reactions (see shaded entries in Table 2), were omitted for the simulation results provided in this paper. Simulations 1 and 3 have also been computed with the full kinetics set and were found to produce minor differences to the resulting axial pressure profiles, verifying that the reduced set could be used.

Mixing limited reactions, via the standard EDC available in Wind-US, are applied to both of the single-step, forward-only reactions. The EDC approach limits chemical reactions rates by the rate at which fuel and oxidizer are turbulently mixed at the micro-scale. EDC provides a limiting rate estimate based on the rate at which eddies at the Kolmogorov scale dissipate into heat, which is applied to each cell based on local turbulence quantities and fuel and oxidizer concentrations, as described below. Preliminary investigations found that simulation results without the EDC activated resulted in poor comparisons with experimental data (i.e., significantly higher peak pressures are obtained).

Table 2. Quasi-Global Chemical Kinetics Model for C2H4 and CH4 Fuel Combination

#	Reaction	S_f	D_f/K_B (K)	C_f (cm^3/g-mol/s/K^{S_f})$^{\text{Order-1}}$	Conc. Exp.	
	Fuel-O2 Single-Step Reactions					
1	C2H4 + O2 ⇒ 2CO + 2H2 (*)	0.0	15098	4.3E+12	0.1	1.65
2	CH4 + 0.5O2 ⇒ CO + 2H2 (*)	0.0	15098	2.3E+07	-0.3	1.30
	CO and H2 Kinetics					
3	H + O2 + M ⇔ HO2 + M	0.0	-505.1	1.5E+15		
4	H2O2 + M ⇔ 2OH + M	0.0	22890	1.2E+17		
5	CO + O + M ⇔ CO2 + M	0.0	2070	5.9E+15		
6	OH + M ⇔ O + H + M	-1.0	52370	8.0E+19		
7	O2 + M ⇔ 2O + M	0.0	58080	5.1E+15		
8	H2 + M ⇔ 2H + M	0.0	48480	2.2E+14		
9	H2O + M ⇔ H + OH + M	0.0	53030	2.2E+16		
10	H + O2 ⇔ O + OH	0.0	8484	2.2E+14		
11	H2 + O ⇔ H + OH	1.0	4495	1.8E+10		
12	O + H2O ⇔ 2OH	0.0	9293	6.8E+13		
13	OH + H2 ⇔ H + H2O	0.0	2576	2.2E+13		
14	O + HO2 ⇔ O2 + OH	0.0	505.0	5.0E+13		
15	H + HO2 ⇔ 2OH	0.0	959.6	2.5E+14		
16	H + HO2 ⇔ H2 + O2	0.0	353.5	2.5E+13		
17	OH + HO2 ⇔ H2O + O2	0.0	505.1	5.0E+13		
18	2HO2 ⇔ H2O2 + O2	0.0	505.1	1.0E+13		
19	HO2 + H2 ⇔ H2O2 + H	0.0	9444	7.3E+11		
20	H2O2 + OH ⇔ H2O + HO2	0.0	909.0	1.0E+13		
21	CO + OH ⇔ CO2 + H	1.3	-404.0	1.5E+07		
22	CO + O2 ⇔ CO2 + O	0.0	18990	3.1E+11		
23	CO + HO2 ⇔ CO2 + OH	0.0	11970	1.5E+14		

Species: C_2H_2, CH_4, O, O_2, CO, CO_2, H, H_2, OH, H_2O, HO_2, H_2O_2, N_2
(*) Mixing-limited reaction

Chemical Kinetics Implementation Notes:

- The forward reaction rate is calculated using an Arrhenius expression:
  $k_{f,lam} = C_f T^{S}_f e^{-(D_f / K_B)T}$
- The backward reaction rate is calculated from the equilibrium constant, K:
  $k_b = k_{f,lam} / K$
- The mixing-limited forward reaction rate is computed using the Eddy Dissipation Concept:
  $k_{f,mix} = C_{edc} (\rho/M_1) C_\mu \omega \min \{[S_1], [S_2] (c_1 M_1) / (c_2 M_2)\}$
  where [S], M, and c are the concentrations, molecular weight, and stoichiometric coefficient for the fuel ("1") and oxidizer ("2"). The standard C_{edc} value of 4.0 has been selected. Menter's SST model provides the local turbulent frequency, ω, *and* C_μ is 0.09.
- The smaller of $k_{f,lam}$ and $k_{f,mix}$ is selected as the forward reaction rate for mixing-limited reactions.

IV. Results

A. Mach 5.84 Grid Sensitivity Study

A grid convergence study was initially conducted for flow conditions which approximate the Mach 5.84 case (i.e., case #1). Fuel injector inflow stagnation pressures have been chosen for both the pair of primary injectors and the pair of secondary injectors, respectively, to mimic the experimental situation where each injector in a pair is fed from the same manifold. The stagnation temperature is approximated as 540°R, or room temperature. These injector stagnation pressures are set to produce an overall equivalence ratio which closely matches that reported from the experiment for the medium grid level (i.e., $\Phi = 0.65$). However, the exact fuel split between the primary and secondary pairs was not scrutinized to closely match experiment since the main purpose of this exercise is to evaluate grid sensitivity, and not to validate results against experiment. Once the pressure levels had been identified for the medium grid level, these boundary settings remain constant for the coarse and fine grid levels to provide an appropriate measure of grid sensitivity. Note that each level of grid fineness involves systematically doubling the number of cells in *i*-, *j*-, and *k*- coordinate directions, or an eight-fold increase in the cell count.

Table 3. Summary of Equivalence Ratios for Coarse, Medium, and Fine Grids

	$\Phi_{Primary}$	$\Phi_{Secondary}$	Φ_{Total}
Coarse	0.267	0.325	0.592
Medium	0.246	0.428	0.674
Fine	0.234	0.499	0.734

Table 3 summarizes the resulting equivalence ratios for each injector pair and grid level. The fine grid case converged to a ϕ_{Total} of approximately 0.72, compared to the experimental value of 0.65. This discrepancy is due to an increase in the effective circular injector face area, and changes to the flowfield solution just downstream of the injectors, both due to increased grid

fineness. The secondary injectors, with a smaller diameter, are choked and mass flows rate are both stable and consistent among the pair in each case. The primary injectors, however, have a much larger diameter and are not choked, resulting in significantly different mass flow rates within the injector pair. More specifically, the fuel injector nearest the sidewall experiences a lower pressure immediately downstream of the injector hole, which resulted in higher fuel mass flow rates than for the injector nearer the centerline. For these simulations, the mass flow rates through the primary injectors have approximately a 35%/75% split. Strong flow oscillations also occurred in the primary injectors, which greatly increased the cpu time needed to reach solution convergence and presented issues to numerical stability.

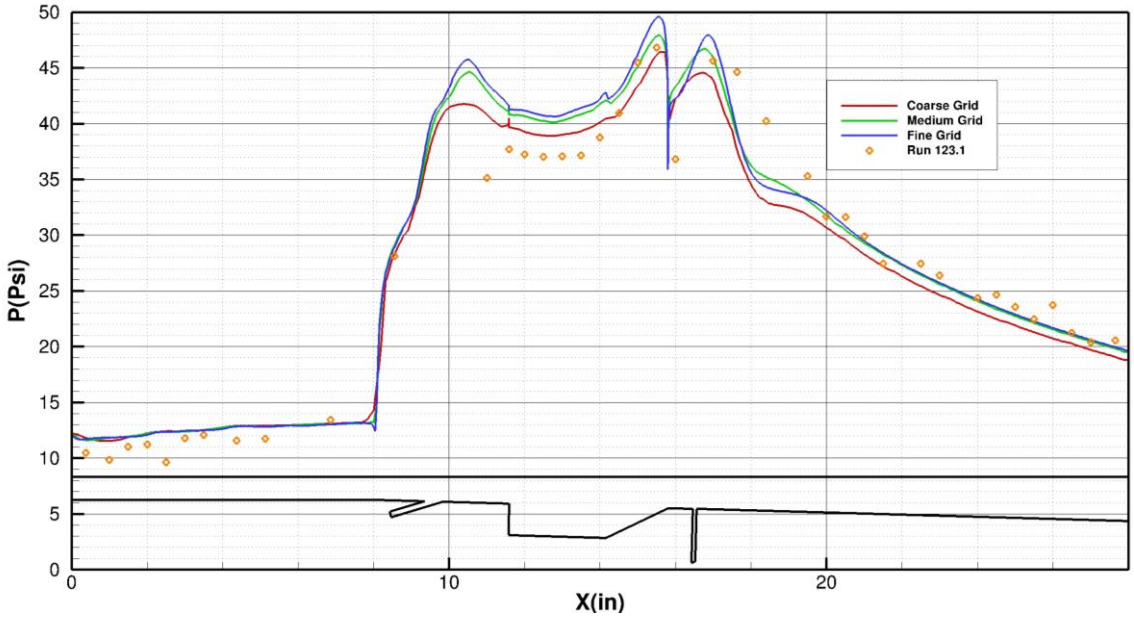

Figure 4. Axial pressure distributions along the symmetry plane for Grid Sensitivity

Figure 4. Axial pressure distributions along the symmetry plane for Grid Sensitivityshows the axial pressure distribution for the baseline Mach 5.84 case for all three grid levels. The results suggest that grid independence is nearly obtained since the medium and fine grid level results are more closely matched than the coarse and medium results. The differences for the peak pressure regions, near the secondary injectors, are the most pronounced, but the trend suggests that another

extra-fine grid level would result in less than a 1 psi difference in the pressure profile compared to the fine level result. The experimental data is included in Figure 4. Axial pressure distributions along the symmetry plane for Grid Sensitivity for reference, but is not directly comparable due to the differences in the primary/secondary fuel split. Based on these results, we chose to produce and disseminate only medium grid level results in the subsequent work described in this paper.

B. Turbulent Schmidt (Sct) = 0.6

Figure 5. Centerline Pressure Distributions for Mach 5.84 (top), 6.5 (mid), and 8.0 (bottom)is the centerline axial pressure distribution taken along the symmetry plane along the cavity of the flowpath, for the three Mach numbers simulated (Cases 1-3). In each case, the injector pair stagnation pressure has been modulated to closely match the fuel contribution measured in the experiment. Reasonable agreement is achieved and the average pressure error (i.e., based on integration of absolute pressure error along the wall surface). The average pressure error for the Mach 5.84, 6.5, and 8.0 cases is approximately 9.0%, 7.5%, and 23%, respectfully. In the Mach 5.84 case the model slightly over predicts the peak pressure which occurs around the location of the primary (upstream) injectors. This effect is more exaggerated if the mixing-limited EDC approach is omitted (not shown). This peak pressure exaggeration is less noticeable in the Mach 6.5 case. Both Mach 5.84 and 6.5 experience similar peak pressure values. It should be noted that they are run with the same facility nozzle. The results below have been obtained with equivalence ratios which match within several percent of experimental data. The Mach 5.84 case saw quasi-steady convergence and an averaged pressure profile is presented, as well as used for error calculations.

The Mach 8.0 case exhibits large disagreement in the peak pressure, which will be discussed in more detail below. There is also significantly lower pressure at the isolator entrance (i.e., from the supply nozzle), which is thought to be likely due to a combination of nonequilibrium thermodynamics (vibrational) effects within the supply nozzle, and thermal deformation of the supply nozzle [17]. Interestingly, this large pressure offset seems to "propagate" for the bulk of

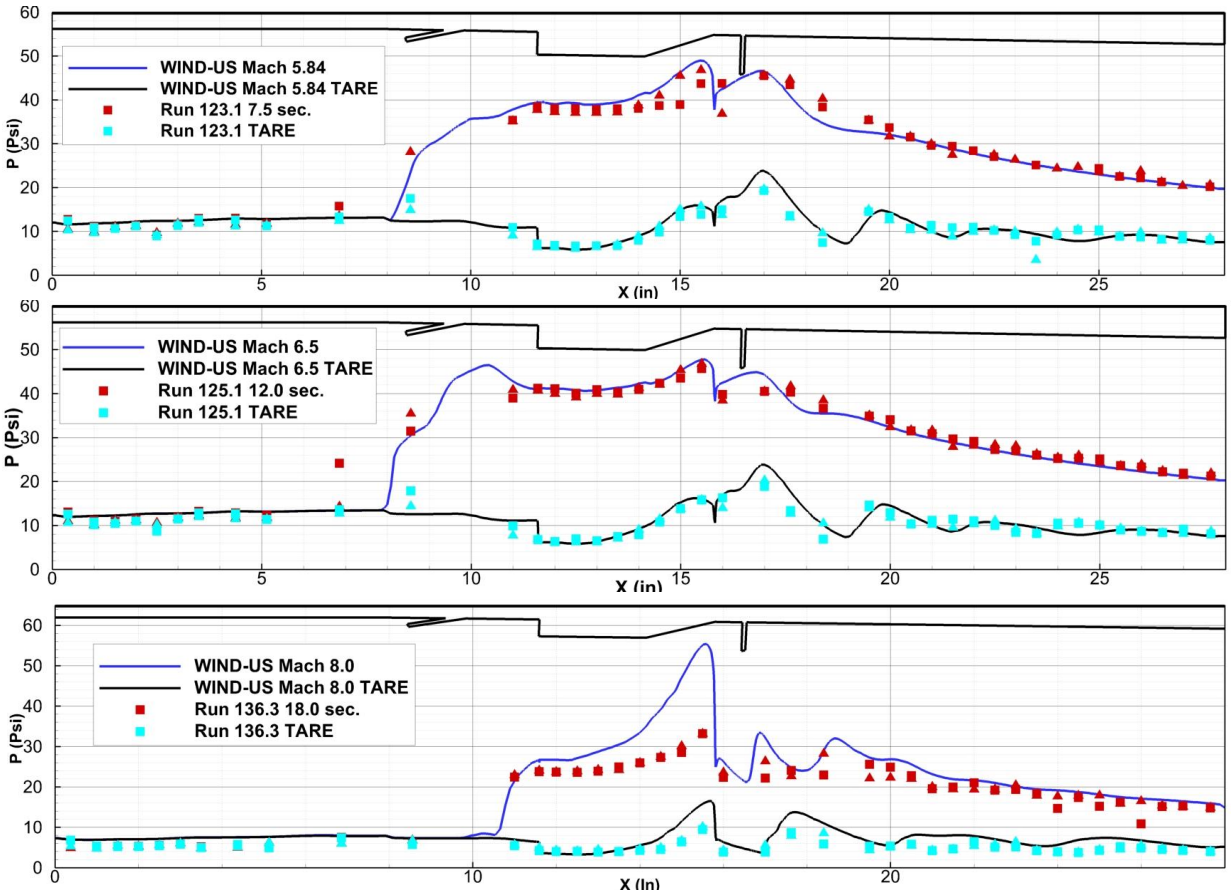

Figure 5. Centerline Pressure Distributions for Mach 5.84 (top), 6.5 (mid), and 8.0 (bottom)

the Mach 8 TARE runs, with the exception for x = 11 to 14 inches. This offset doesn't appear in the other TARE runs which exhibit better agreement. So, this pressure offset from the supply nozzle may be causing a large portion of the pressure error in the Mach 8 runs (both TARE and reacting), except near x of 15 inches.

Figure 6 compares the pressure profile given above for the Mach 8 case along the centerline, with a pressure profile taken along the endwall corner (i.e., on opposite edge of the same wall). It is notable that this profile agrees much better with experiment in the peak pressure region. It turns out that the large peak pressure at x = 15 is confined to a small region along the centerline, and that the profile along the opposite edge is more representative of the pressure distribution along the surface. Consequently, the agreement between computations and experiment may have been much better across the entire surface rather than along the symmetry line only. However, there is not sufficient off-centerline experimental data available to make this comparison.

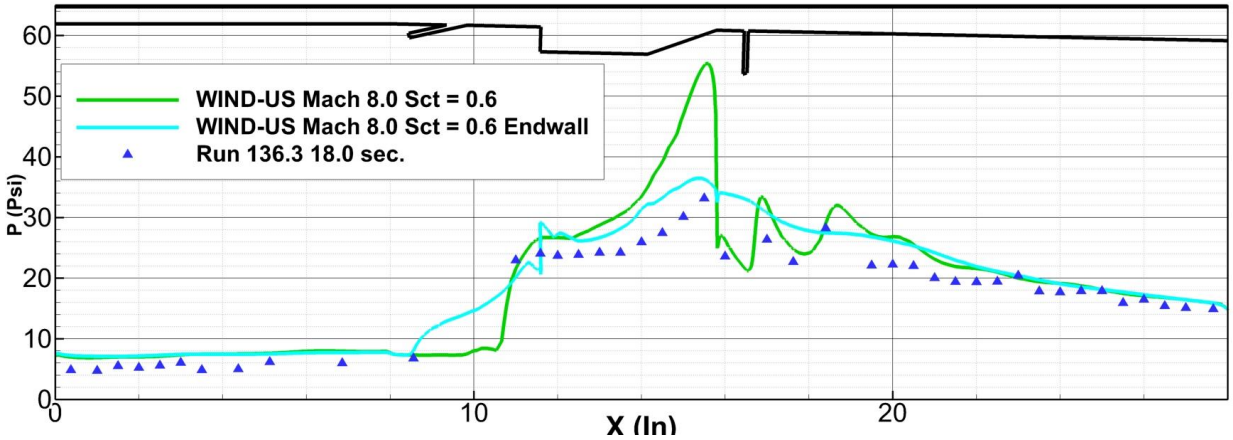

Figure 6. Comparison of wall pressure predicted along symmetry plane and endwall with experiment

Figure 7 shows contours of Mach number, along the symmetry plane as well as planes normal to the core flow for the Mach 5.84, 6.5, and 8.0 cases. The flow structure for the Mach 5.84 and 6.5 cases is very similar, as expected due to using the same nozzle, and exhibits supersonic flow throughout the bulk flow. The Mach 8 case exhibits a slightly different flow structure, with the core supersonic flow being more diamond shaped than the rectangular form of the lower Mach number cases. This difference is related to the corner flow separation upstream of the primary injectors also evident in Figure 7. Combustion products travel upstream into the isolator via this corner separation.

Table 4. Integrated Error Values

Total Error			
Sc_t	Mach #		
	5.84	6.5	8
0.6	7.47%	10.56%	23.20%
0.6*	-	-	14.37%
0.7	7.49%	10.73%	22.35%
TARE	15.68%	15.35%	35.32%

*Numerical pressures are decreased by 2 psi to adjust for disagreement in isolator entrance pressure

Table 4 shows the error values which have been integrated over the CFD pressure profile using linear interpolation between experimental pressure taps. The Mach 5.84 and 6.5 reacting flow cases produce modest errors of roughly 10% or less. The Mach 8 reacting case provides poor accuracy unless a pressure offset is included to account for the large difference in pressure at the isolator entrance, and assuming that offset propagates thru the flowpath. The tare accuracy levels of ~15% for Mach 5.84 and 6.5 correspond to an average error of ~1.5 psi. The percentage error for wall pressure is integrated using the x-coordinate of each wall node, as follows:

$$\boldsymbol{ERROR} = \frac{\sum_{X_0}^{X_{last}} \left| \frac{\boldsymbol{P_{CFD}}}{\boldsymbol{P_{exp}}} - \mathbf{1} \right| * (\boldsymbol{\Delta X})}{\boldsymbol{X_{last}} - \boldsymbol{X_0}} * \mathbf{100}\%$$

This approach is a conservative calculation of error, as it includes local weighting to the overall error.

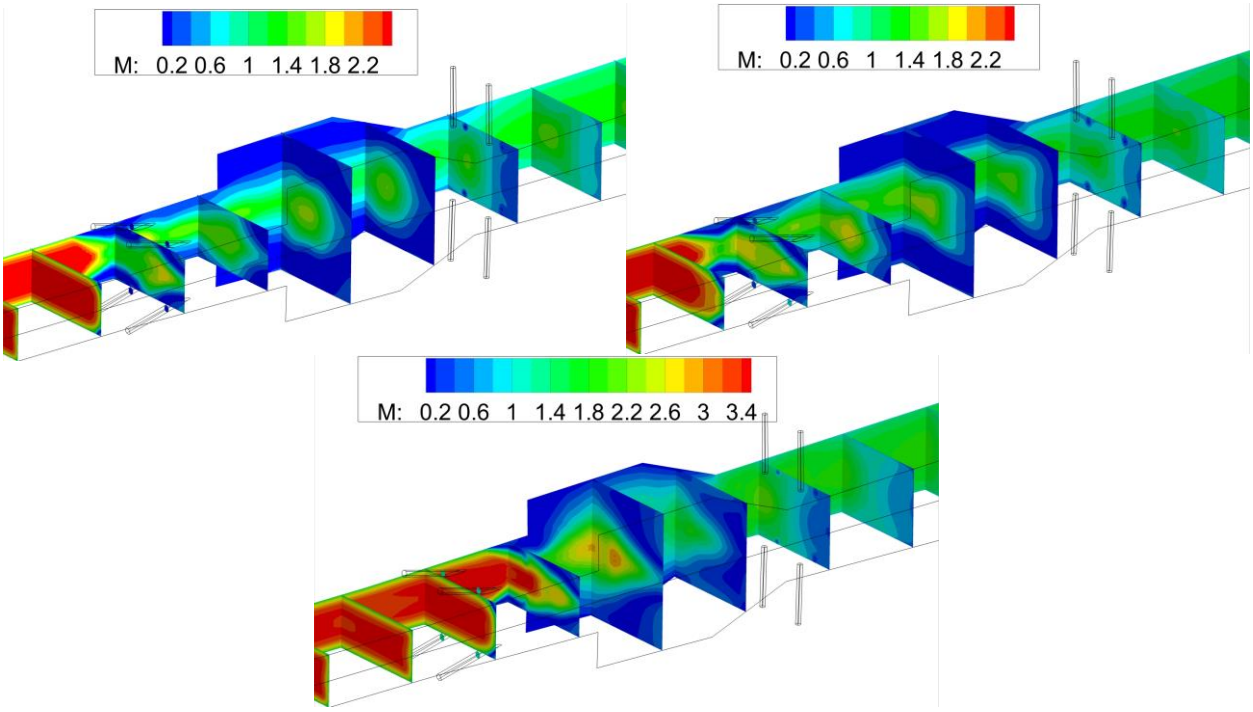

Figure 7. Mach Number Contours for Mach 5.84 (top left), Mach 6.5 (top right), and Mach 8.0 (bottom center)

Figure 8 shows the variation of the mass flow weighted Mach number taken at 15 evenly spaced slices axially throughout the flowpath, using Tecplot 360s integration tool, for cases 1-3. Storch [3] suggested that the engine is in ramjet mode during this Mach 5.84 condition, based on one dimensional Mach number profiles. As seen in Figure 8, the present results for Mach number also predict ram-mode with a drop slightly below unity for roughly three inches near the end of the combustor and beginning of nozzle. Another indication of ram-mode for the two lower speed cases, Mach 5.84 and 6.5, from Figure 9, is that combustion occurs upstream of the primary injectors. The Mach 8 case is predicted to be in scram-mode as the mass flow weighted Mach number never drops below unity, and no combustion is evident upstream of primary injectors in Figure 9.

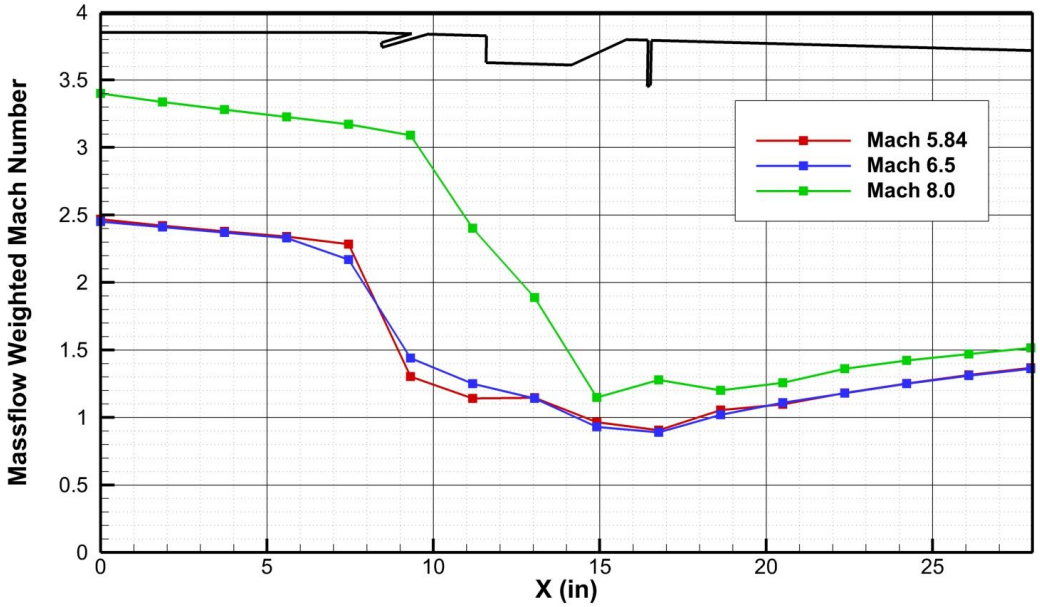

Figure 8. Axial Profile of Mass flow Weighted Mach Number

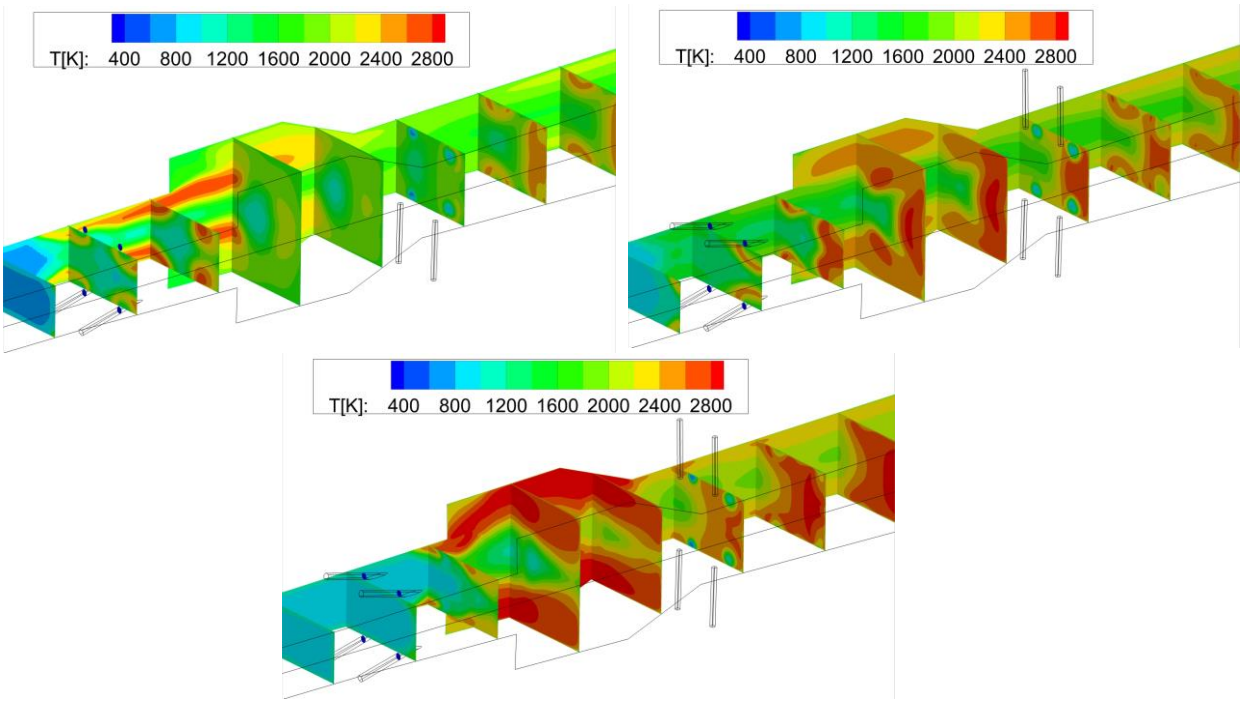

Figure 9. Temperature Contours for Mach 5.84 (top left), Mach 6.5 (top right), and Mach 8.0 (bottom center)

Figure 9 shows temperature contours for the three simulated flight Mach numbers. The two lower speed cases, Mach 5.84 and 6.5, exhibit peak temperatures of around 2600 °K, which is expected to produce minor levels of nitrous oxides. The potential for NOx production in the Mach 8.0 case is only somewhat elevated due to peak temperatures of around 2800 °K. Hence, exclusion of NOx chemical pathways in the present chemical kinetics approach, appears to be justifiable.

Figure 10 shows the percent complete combustion based on amount of CO_2 produced compared to the total amount which could be formed as calculated from the total fuel being supplied, assuming complete combustion to purely H_2O and CO_2 products. The two lower Mach number cases show strong similarity through the cavity due to the similarity in flow structure through the isolator and first part of the cavity, as seen in Figure 7 and Figure 9. Both 5.84 and 6.5 cases show flow separation upstream of the primary injectors allowing for combustion to start at a similar location upstream of the primary injectors, in contrast to the Mach 8 case for which combustion starts just downstream of this injector. The latter supports the notion that the Mach 8 case is in scram-mode.

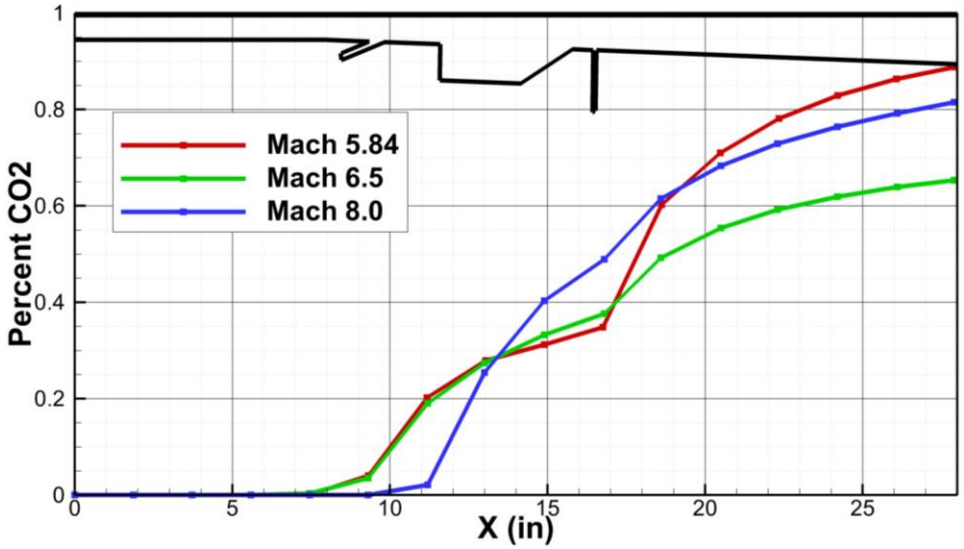

Figure 10. Axial Profile of Percent Complete Combustion

C. Turbulent Schmidt Sensitivity

Figure 11 illustrates the relatively weak sensitivity of the pressure profiles for the three simulated flight Mach numbers to a change in the turbulent Schmidt number. The baseline results with a Sc_t of 0.6 are compared to results obtained with a Sc_t of 0.7. Slightly lower peak pressure levels are obtained for Sc_t of 0.7 for all three cases. The latter is expected since a higher Sc_t suggests a reduction in the species mixing needed for combustion. For the 5.84 case quasi-steady convergence is achieved for both turbulent Schmidt numbers. For the cases of Sc_t of 0.6 the variation in pressure is much larger than in the case of Sc_t of 0.7, with fluctuations between 5-10 psi depending on location. Conversely using a Sc_t of 0.6 resulted in unsteady pressure variations of less than 3 psi.

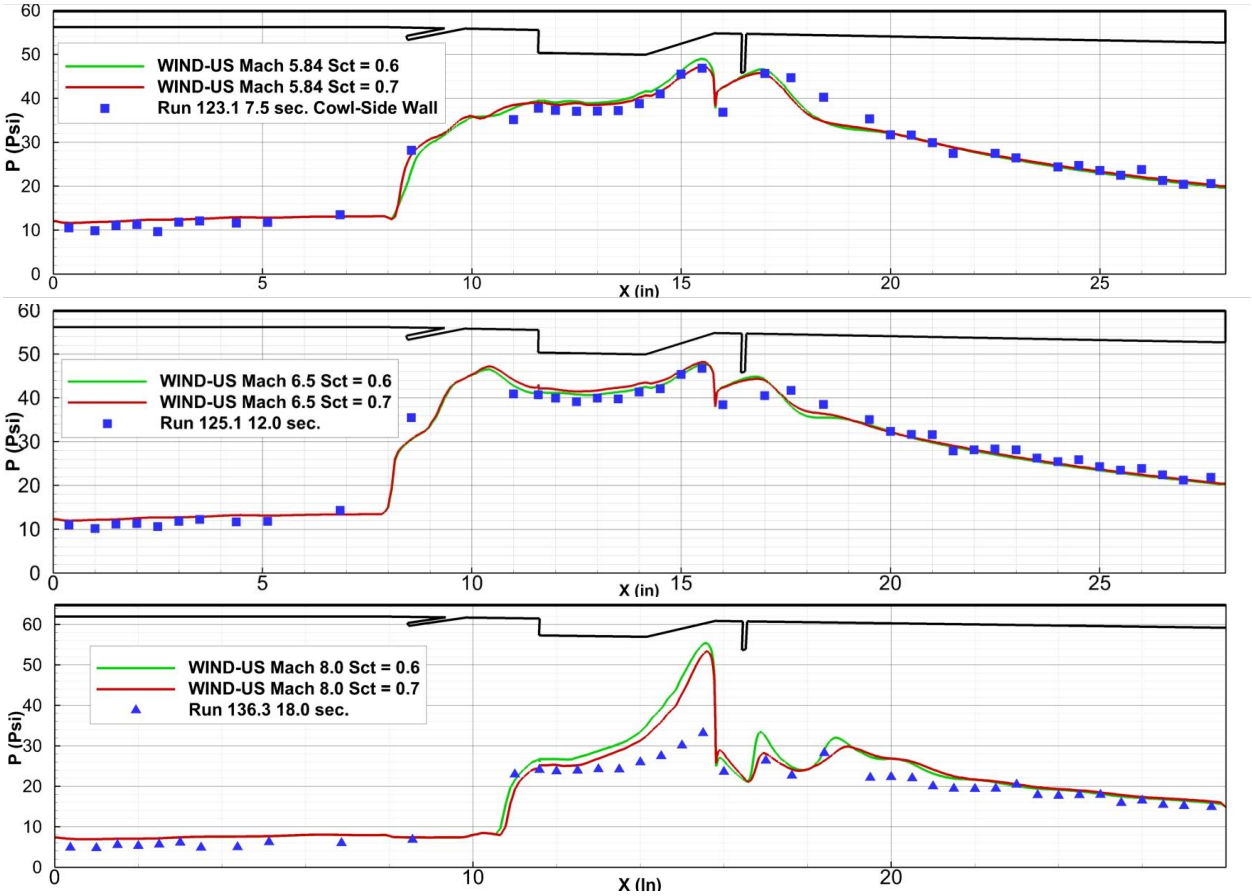

Figure 11. Comparison of Centerline Pressure Distributions vs. Turbulent Schmidt for Mach 5.84 (top), 6.5 (mid), and 8.0 (bottom)

D. Eddy Dissipation Concept

Figure 12 illustrates the effect of the turbulent mixing-limit on combustion. The contour variable is the reduction in the destruction rate of fuel for ethylene, C_2H_4 (top) and methane, CH_4 (bottom) for cases 1-3. The red regions indicates very strong limiting of the fuel destruction rate due to turbulent mixing. For the Mach 5.84 case, the effect on ethylene destruction is dramatic in the bulk flow when comparing these reduction levels to the listed, peak laminar destruction rates for the entire combustor flow field. However, the mixing-limiting effect (i.e., reduction in destruction rate) for methane is shown to be an order-of-magnitude smaller. The latter is due to

the comparatively low laminar destruction rates for methane versus ethylene, as observed from the reaction constants in reactions #1 and #2 in Table 2.

At Mach 6.5 and Mach 8.0 the reduction in destruction rate due to mixing-limiting for ethylene becomes only slightly larger, likely due to increased turbulence production. However, relative to the rapidly increasing laminar rates, the mixing-limiting effect appears to be less significant as simulated Mach number increases.

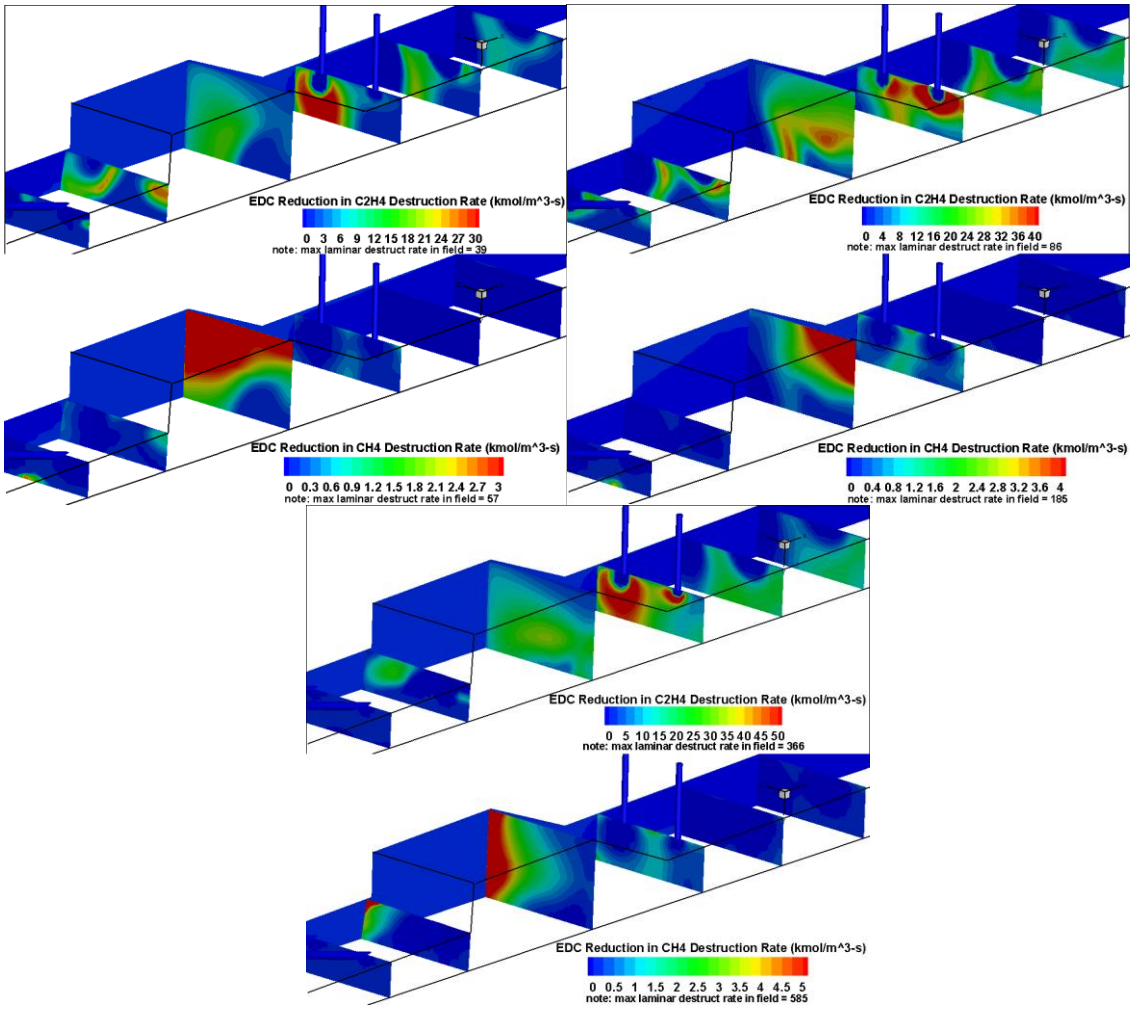

Figure 12. Reduction in Rate of Fuel Destruction due to EDC Mixing-Limit for Mach 5.84 (top left), Mach 6.5 (top right), and Mach 8.0 (bottom center)

E. Effect of Vitiation

I. HIFiRE II

It was desired to take an initial look into the effect that carbon dioxide and water have on the combustion process within a scramjet engine. Previous works have shown that the expected effect of water vapor on combustion is a decrease in combustor pressure [6]. Tatman et al. [18] recently looked experimentally at the effect of vitiation in a hydrocarbon fueled scramjet, and state that the water vapor can both effect the thermodynamics as well as acting as a third-body reaction. In particular Tatman singles out the formation of HO_2 as a significant factor in the vitiation effect. Chinitz and Erdos [19] measured numerically, though the NASA LSENS code [20], the effect vitiation had on total combustion time, and ignition delay for several different fuels and different concentrations of two different vitiates. The results demonstrated that the different vitiates had varying levels of pressure reduction and ignition delay, over subsequent temperature ranges, and vitiate concentrations. The effect seen varied significantly for certain combinations of vitiate and flow conditions, increasing the ignition delay by 40% in some cases.

Mach 5.84 flight enthalpy was used with three different vitiation configurations evaluated. Clean air, 10% H_2O, and 10% CO_2 cases were run to gain an initial estimate at the effects each vitiate would have. Vitiation was measured as a percent mole fraction, and as such 10% of the nitrogen was replaced directly with the other vitiate. Enthalpies were not recalculated for the new air mixtures, but kept the same as clean air (i.e. the same total pressure and temperatures were used). The resulting stoichiometric equations were:

$$(\,0.36CH_4 + 0.64C_2H_4) + \alpha(0.21O_2 + \,0.79N_2) \rightarrow \beta H_2O + \gamma CO_2 + \epsilon N_2$$

$$(0.36CH_4 + 0.64C_2H_4) + \alpha(0.21O_2 + 0.69N_2 + 0.1CO_2) \rightarrow \beta H_2O + \gamma CO_2 + \epsilon N_2$$

$$(0.36CH_4 + 0.64C_2H_4) + \alpha(0.21O_2 + 0.69N_2 + 0.1H_2O) \rightarrow \beta H_2O + \gamma CO_2 + \epsilon N_2$$

The resulting values for the stoichiometric coefficients are presented in Table 5 below.

Table 5. Stoichiometric Coefficients

	α	β	γ
Clean	12.571	1.64	2
10% H_2O	12.571	1.64	3.257
10% CO_2	12.571	2.897	2

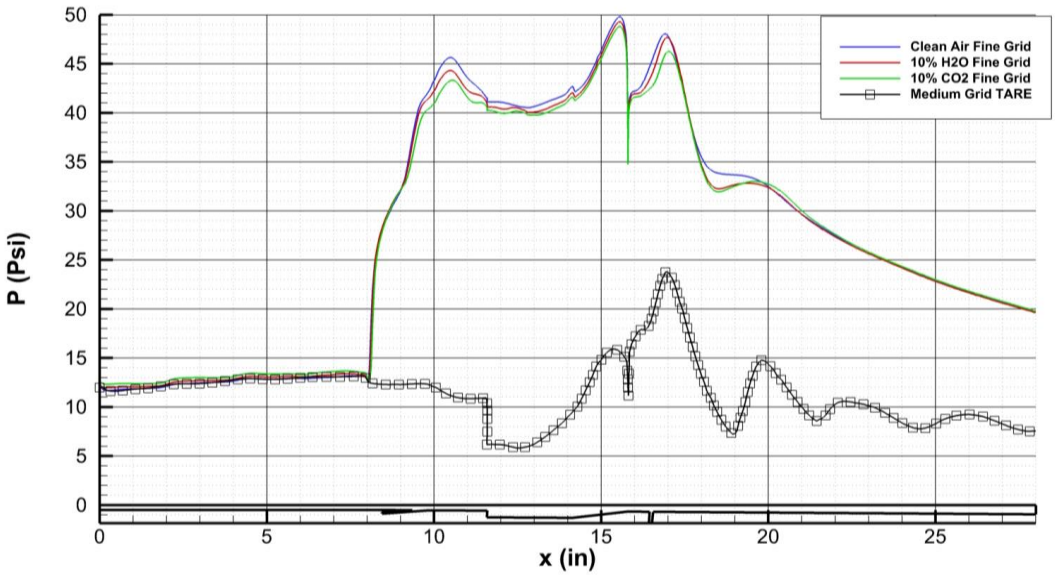

Figure 13. Axial Pressure Distribution for Vitiated Air Cases

For the cases within this vitiation study, the equivalence ratio was typically around 0.75 with a 0.25/0.5 split, front to rear. Unfortunately there was no experimental data to make a direct comparison, so the study is only academic in nature. Figure 13 shows the effect of water and CO2 vitiation at one flight configuration. A slight but noticeable decrease in pressure is seen immediately following both primary and secondary injectors. However the pressures tend to

equalize as the flow moves downstream. Just aft of the primary injectors the CO2 vitiated air sees a roughly 7% drop in peak combustor pressure compared to the clean air, the H_2O vitiated air sees a smaller 4.5% drop in pressure.

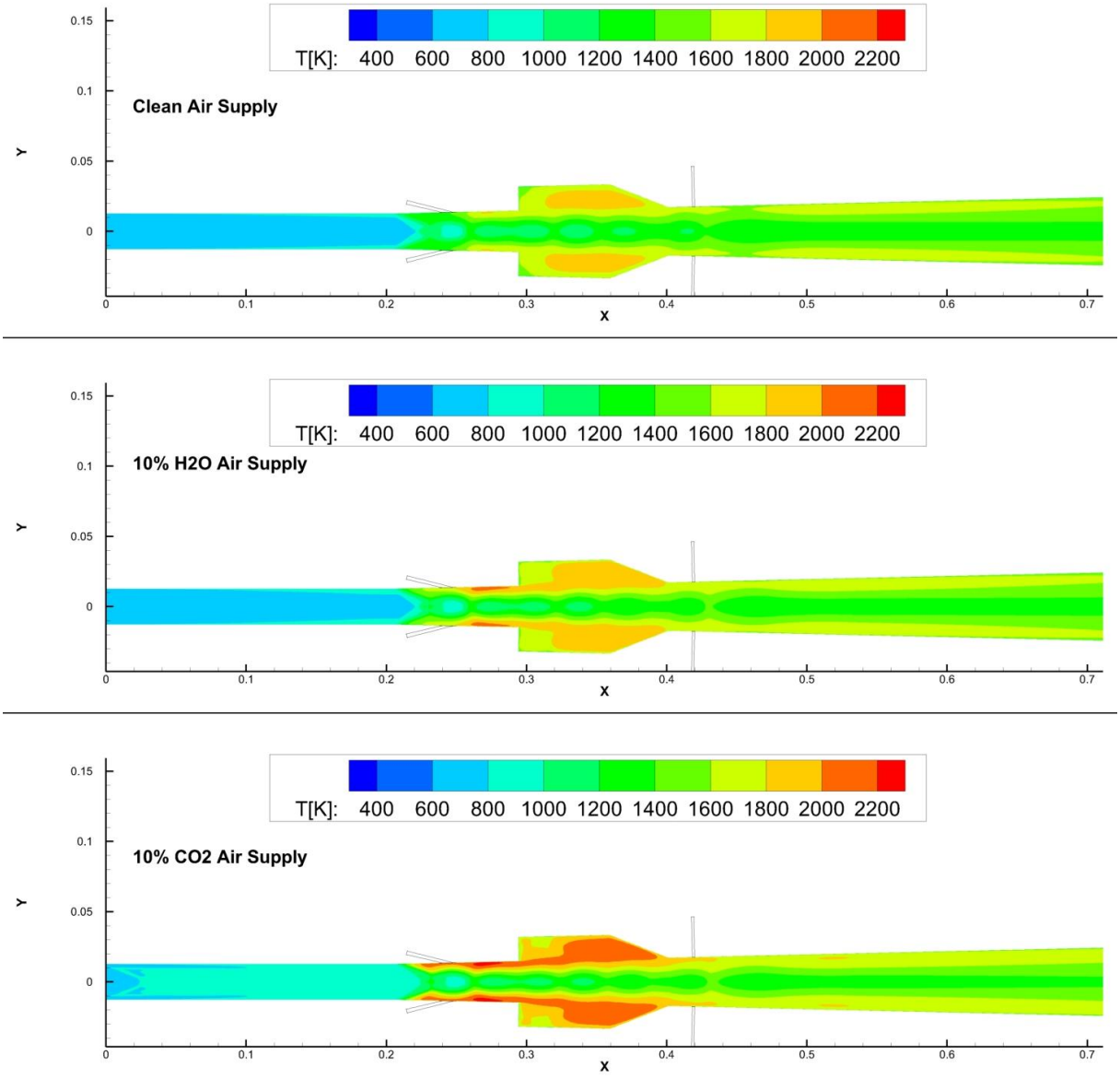

Figure 14. Temperature Contours at the Center-Plane for Vitiated Air Cases

Immediately before the downstream pressure increase the 3 cases equilibrated to within 2% of the clean air peak combustor pressure. Just aft of the secondary injectors a similar phenomenon is seen

with drops in combustor pressure seen in both CO_2 and H_2O vitiation. By the exit of the flowpath, the pressure have returned to within 0.5 psi of one another. Another slight difference which can be seen in Figure 13 is that the clean air case sees the pressure increase slightly forward of the vitiated cases. The decrease in combustor pressure and delay in ignition time agree with the works of Vyas, Tatman, and Chinitz[6,18,19]. Figures 14 and 15 show contour slices, of temperature and hydrogen mole fraction respectively, from the center plane of the same cases shown above in Figure 13. Interestingly the temperatures in the cavity at the center plane are higher for the vitiated cases than they are for the clean case. This could possibly be explained by Figure 15 which shows the hydrogen mole fraction, which are higher for the vitiated cases. This increase of hydrogen upstream of the cavity would lead to higher entrainment of fuel in the form of hydrogen, into the cavity serving as a flame holder.

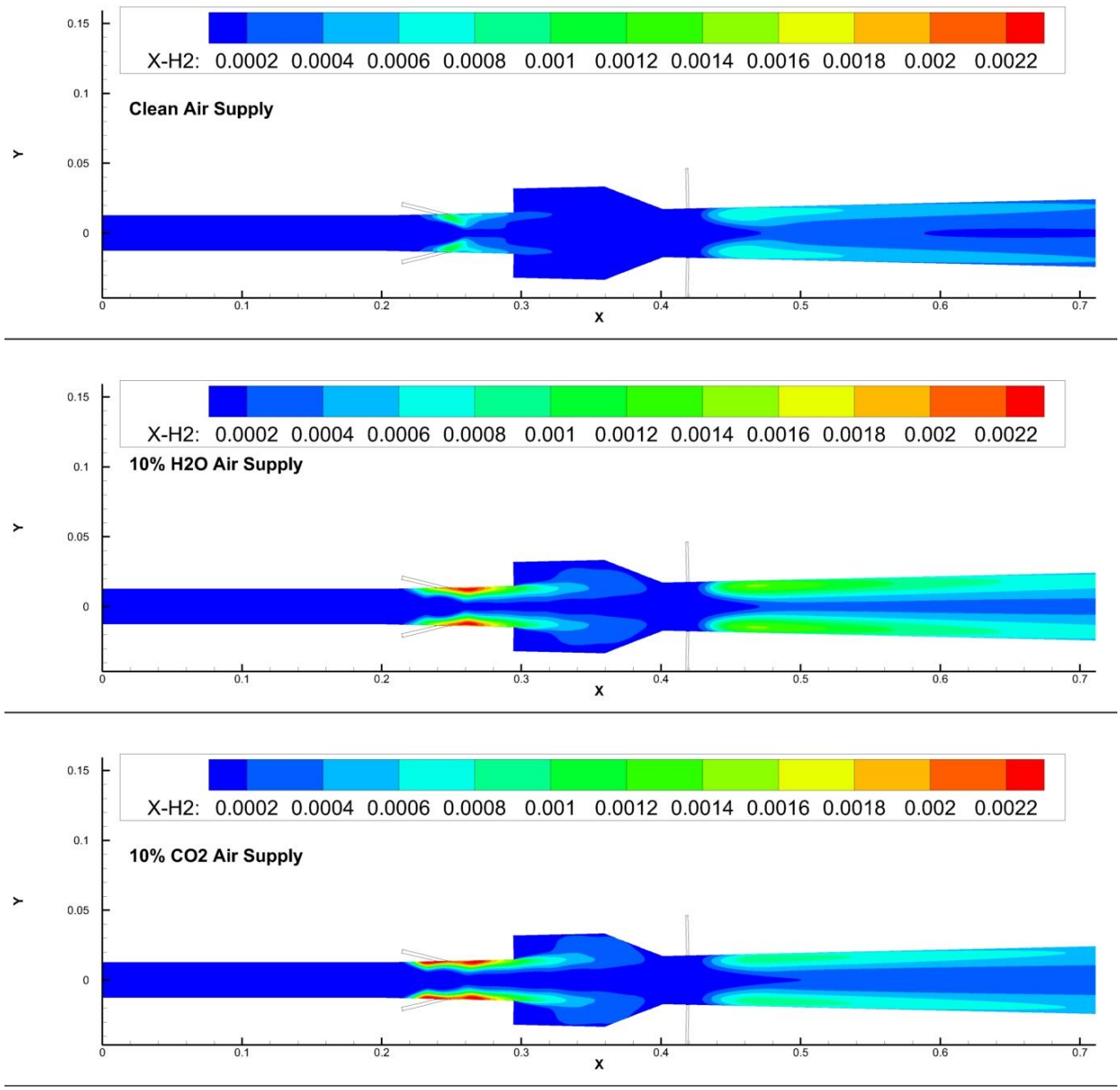

Figure 15. Mole Fractions of H_2 for Vitiated Air Cases

II. Burrows-Kurkov Cases

In an attempt to better understand what causes vitiation to decrease combustor pressure, a systematic deconstruction of the chemical kinetics used, was performed on the classic Burrows and Kurkov vitiated air combustion case. Modified chemistry files were developed and utilized to

isolate a) the thermodynamic effect of water, b) the 3rd body efficiency effect of water on H_2-O_2 chemical kinetics, and c) the chemical kinetics effect of water (i.e., other than as 3rd body effect). This was accomplished by adding each subsequent effect into the chemical kinetics set. Figure 16 shows the temperature contours of the cases which isolate the effects.

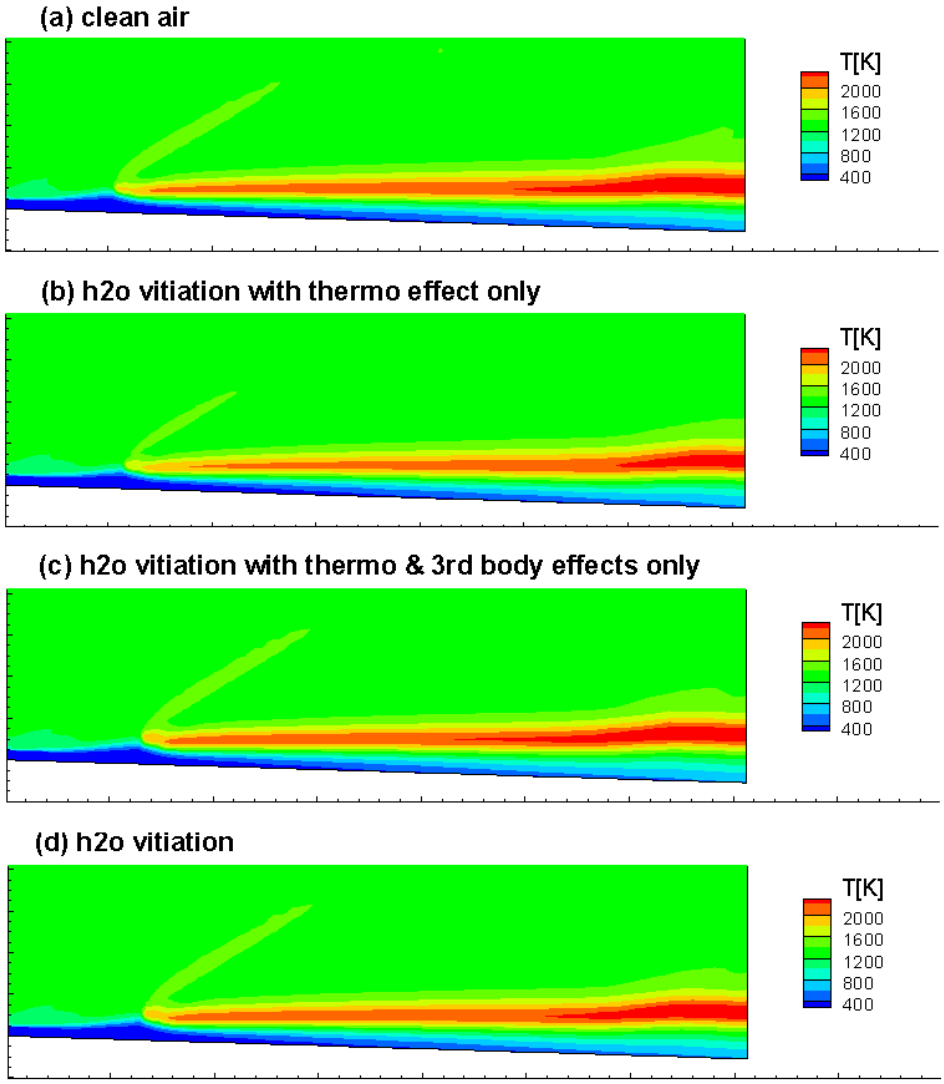

Figure 16. Contours of Temperature for Isolated Effects in the Burrows-Kurkov Vitiated Combustion Cases

Figure 16a shows the clean air version of the Burrows-Kurkov case. A black line is added to show the leading edge of the flame for the clean case. Figure 16b shows the effect of H_2O vitiation with only thermodynamic effects present. This was achieved by adding a placeholder species, H_2OX which has the thermodynamic properties of H_2O without the third-body efficiency of H_2O which is significantly higher than most species. In the Peter and Rogg kinetics H_2O has an efficiency of 6.5 compared to O_2 which has an efficiency of 0.4. This H_2OX specie is then used as the vitiate at the inflow. H_2OX cannot be created or destroyed as there are no reactions for the extra specie in the chemistry file. There is a slight shift aft in flame front from the thermodynamic effects alone, from the water vapor absorbing more heat from the flow than would be otherwise not be absorbed reducing the temperature, and therefore the laminar reaction rates as well. It should be added that a control case, where H_2OX was exactly the same as H_2O was also performed to ensure the same results would be obtained as the normal Peters and Rogg kinetics file.

Figure 16c shows the effect when the higher third-body efficiency is added. For this case the third body efficiencies are increased back up to the normal level of 6.5. There is a further increase in ignition delay seen with the third body effects turned back on. However there seems to be a slight increase in the exit temperature. The higher level for the efficiency of H_2O in third-body reactions will cause an increase in the chain-initiation reactions and chain-terminating reactions (reactions 3-9 from Table 2), which could help produce some long-lived radicals which delay the ignition. However, once the reaction is started, the higher third-body efficiencies will increase the rate at which combustion products are formed, increasing the local temperature. This is confirmed as a larger high temperature range is seen in Figure 16c than in Figure 16b.

Figure 16d provides result with full vitiated combustion kinetics. The result shows a slightly larger ignition delay than with only thermodynamics and third-body efficiencies. It is

speculated that in the fully vitiated case, H_2O is decomposed into other vitiates, which have smaller third-body efficiencies, and slow the rate of combustion slightly. Figure 17 shows the temperature profile along the vertical distance along the exit plane and shows similar trends. Clean air produces the thickest and hottest flame, while the thermodynamic only flame is the smallest and coldest. Reintroducing the third-body efficiencies the width and temperature of the flame increases but not to the extent of the clean air.

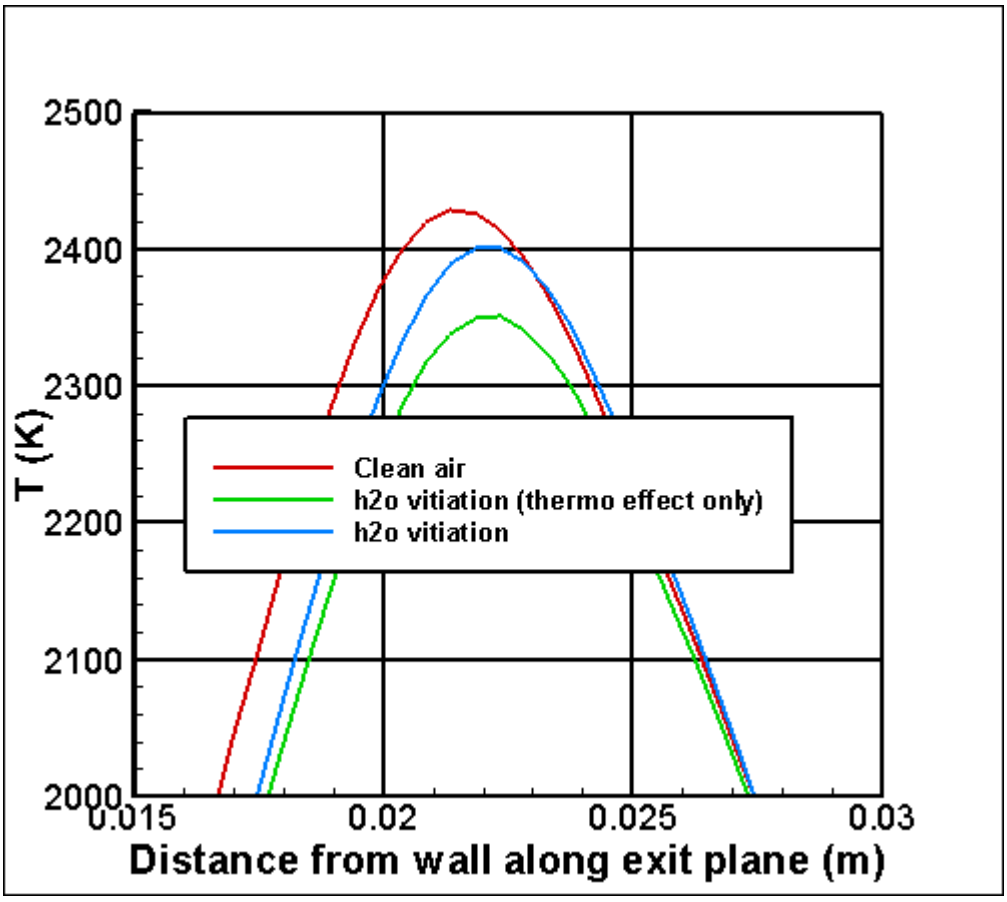

Figure 17. Temperature Profiles at the Exit for Isolated Effects in the Burrows-Kurkov Vitiated Combustion Cases

V. Summary and Conclusions

A Wind-US model featuring a mixing-limited, quasi-global chemical kinetics approach for an ethylene-methane fuel mixture is shown to produce good predictions of pressure profiles within the HIFiRE 2 flowpath based on direct comparison with HFDCR experimental data for flight Mach numbers of 5.84, 6.5, and 8.0. Average static pressure error level between the numerical predictions and corresponding experimental measurements are found to be less than 10% for Mach 5.84 and 6.5, without calibration of turbulence effects. The comparison at Mach 8.0 is hampered by a large offset in pressure at the isolator entrance due to issues outside of the current numerical model; however, if the offset is removed, good agreement is expected for Mach 8.0 tare and reacting cases, without calibration. The effect of the mixing-limits on combustion are found to be most severe for ethylene in the bulk flow, and especially for the lower simulated Mach numbers. The sensitivity of the results to a small change in turbulent Schmidt is found to be modest for this model.

References

1. Dolvin, D., "Hypersonic International Flight Research and Experimentation Technology Development and Flight Certification Strategy", 16th AIAA/DLR/DGLR International Space Planes and Hypersonic Systems and Technologies Conference AIAA-2009-7228.

2. Jackson K., Gruber M., and Buccellato S. "HIFiRE Flight 2 Overview and Status Update 2011," AIAA Paper 2011-2202, San Francisco April 2011.

3. Storch A., Bynum M., Liu J., and Gruber M., "Combustor Operability and Performance Verification for HIFiRE Flight 2," AIAA-2011-2249, San Francisco April 2011.

4. Georgiadis, N, Mankbadi, M., and Vyas, M., "Turbulence Model Effects on RANS Simulations of the HIFiRE Flight 2 Ground Test Configurations," accepted for publication, SciTech2014, Jan 2014.

5. Nelson, C., "An Overview of the NPARC Alliance's Wind-US Flow Solver," AIAA Paper 2010, Jan. 2010.

6. Vyas, M., Engblom, W., Georgiadis, N., Trefny, C., and Bhagwandin, V., "Numerical Simulation of Vitiation Effects on a Hydrogen-Fueled Dual-Mode Scramjet," AIAA Paper 2010-1127, Jan. 2010.

7. Engblom, W., Bellamkonda, and G., Osborne, J., "Experimental and Numerical Evaluation of Hydrogen Fuelled Dual Mode Scramjet Engine," AIAA Paper 2012-3291, June 2012.

8. Bhagwandin, V., Engblom, W., and Georgiadis, N., "Numerical Simulation of UVA Ramjet/Scramjet H_2-Air Engine using Wind-US Flow Solver," AIAA-2009-5382, Denver, July 2009.

9. Georgiadis, N., Yoder, D., Towne, C., Engblom, W., Bhagwandin, V., Power, G., Lankford, D., and Nelson, C., "Wind-US Code Physical Modeling Improvements to Complement Hypersonic Testing and Evaluation," AIAA Paper-2009-193, Jan 2009.

10. Menter, F. R., "Two-Equation Eddy-Viscosity Turbulence Models For Engineering Applications," *AIAA Journal* 0001-1452 Vol. 32, No. 8 (1598-1605), 1994.

11. Georgiadis N. and Yoder D., "Recalibration of the Shear Stress Transport Model to Improve Calculation of Shock Separated Flows," AIAA-2013-0685, Dallas January 2013.

12. Nichols, R. H., Tramel, and R. W., Buning, P. G., "Evaluation of Two High Order WENO Schemes," AIAA-2007-3920, 2007.

13. Eppard, W., "Damkohler Limiting of Chemical Time Scales," AIAA-2005-1400, Jan 2005.

14. Li, F., Fuhua, M., Yang, V., Lin, K., and Jackson, T., "A Comprehensive Study of Ignition Transient in an Ethylene- Fueled Scramjet Combustor," AIAA-2007-5025, 2007.

15. Magnussen, B.F. and Hjertager, B.H., "On mathematical models of turbulent combustion with special emphasis on soot formation and combustion", *Proceedings of 16th Symp. (Int.) on Combustion,* 719-729, The Combustion Institute, Pittsburgh, PA, 1976.

16. Westbrook C. and Dryer F., "Simplified Reaction Mechanism for the Oxidation of Hydrocarbon Fuels in Flames," *Combustion Science and Technology,* 1981 Vol. 27 pp. 31 – 43.

17. Cabell, Haas, Storch, and Gruber, "HIFiRE Direct-Connect Rig (HDCR) Phase I Scramjet Test Results from the NASA Langley Arc-Heated Scramjet Test Facility**,"** AIAA 2011-2248.

18. Tatman, Rockwell, Goyne, McDaniel, and Donohue, "Experimental Study of Vitiation Effects on Flameholding in a Cavity Flameholder," Journal of Propulsion and Power, Vol. 29, No. 2, 2013

19. Chinitz, and Erdos, "Test Facility Chemistry Effects on Hydrocarbon Flames and Detonations," AIAA Paper 95-2467, July 1995.

20. Radhakrishnan, K. "LSENS: Multipurpose Kinetics and Sensitivity Analysis Code for Homogeneous Gas-Phase Reactions." *AIAA Journal* Vol. 41 No.5 2003, pp. 848-855.

Appendix

A. Sample Wind-US .dat file

```
HiFire ScramJet HFDCR
M = 6.0, SST
Westbroke-Dryer reduced new injectors
/ SPAWNED OUTPUT
spawn "./spawn.sol.copy" frequency 2000
spawn "./spawn.dat.pressure" frequency 500
/spawn "./spawn.contours" frequency 500
/ Inlet Mach number, pressure (psi), temperature (deg R), alpha, beta
freestream static 1.5   58.57   1924.   0.   0.
/Boundary conditions Used to be Zone 7 /zone35
downstream pressure extrapolate zone 35
/ Viscous terms
/turbulence euler
turbulence sst
test 71 5   /5: use curve-fit equations, if outside, extrapolate /3: use nearest limit
tvd factor 2 zone all   /default tvd factor is 3 for roe and hlle second physical
/ Numerics
rhs hllc second upwind
cycles 30000 print frequency 10
iterations per cycle 1
converge order 10
cfl 0.15
crossflow 1

/sequence 2 2 2 zone all
/sequence 1 1 1 zone all
sequence 0 0 0 zone all
/ CHEMISTRY
chemistry
  finite rate
  file westbrook_dryer_reduced.chm local
  species C2H4 0.0 CH4 0.0 O 0.0 O2 0.234 CO 0.0 CO2 0.0 H 0.0 H2 0.0 OH 0.0 H2O 0.0 N2 0.766
  damkohler 100.0
```

```
  EDC 4.0
endchemistry
/ Diffusion settings
prandtl 0.72 0.89
schmidt 0.72 0.60
/ WALL TEMPERATURE
wall temperature 900 zone 1:6
wall temperature 1440 zone 7:15
wall temperature 1440 zone 16:35
/ CLEAN AIR FLOW
arbitrary inflow
  total
  hold_totals
  zone 1
  uniform 0.2 215 2790 0 0
  0.0 0.0 0.0 0.234 0.0 0.0 0.0 0.0 0.0 0.0 0.766
endinflow
/Upstream Injectors
arbitrary inflow
  total
  hold_totals
  zone 36
  uniform 1.0 36.8 540.0 15 0
  0.7568 0.2432 0.0 0.0 0.0 0.0 0.0 0.0 0.0 0.0 0.0
Endinflow
arbitrary inflow
  total
  hold_totals
  zone 37
  uniform 1.0 36.8 540.0 15 0
  0.7568 0.2432 0.0 0.0 0.0 0.0 0.0 0.0 0.0 0.0 0.0
endinflow
/Downstream Injectors
arbitrary inflow
  total
  hold_totals
  zone 38
```

```
  uniform 1.0 97.500 540.0 90 0
  0.7568 0.2432 0.0 0.0 0.0 0.0 0.0 0.0 0.0 0.0 0.0 0.0
endinflow
arbitrary inflow
  total
  hold_totals
  zone 39
  uniform 1.0 97.500 540.0 90 0
  0.7568 0.2432 0.0 0.0 0.0 0.0 0.0 0.0 0.0 0.0 0.0 0.0
endinflow
/ LOADS OUTPUT
loads
pressure offset 0.0
print planes totals frequency 10
reference area 1.0
reference length 1.0
reference moment center 0.0 0.0 0.0
zone 7
  surface i 1 mass force momentum
zone 12
  surface i 1 mass force momentum
zone 35
  surface i last mass force momentum
zone 36
  surface j 1 mass force momentum
zone 36
  surface j last mass force momentum
zone 37
  surface j 1 mass force momentum
zone 37
  surface j last mass force momentum
zone 38
  surface j 1 mass force momentum
zone 38
  surface j last mass force momentum
zone 39
  surface j 1 mass force momentum
```

```
zone 39
  surface j last mass force momentum
zone 25
  surface i 1 mass force momentum
zone 34
  surface i last mass
endloads
end
```

B. Sample Chemistry Input File (.chm)

```
  137      ISPEC
THERMODYNAMIC COEFFICIENTS
 CURVE FITS FROM NASA LEWIS CET86 and  N,NO,CO,CO2 from CHEMKIN DATA

    13     NS
NASA3287
C2H4              Chao,JPCRD,v4,75,p251. Knippers,Ch.Phys,v98,85,p1. TRC.
 2 l 1/91 C   2.00H   4.00    0.00    0.00    0.00 0     28.05376      52500.000
    200.000  1000.000 7 -2.0 -1.0  0.0  1.0  2.0  3.0  4.0  0.0        10518.689
 -1.16361327D+05  2.55486052D+03 -1.60975030D+01  6.62578637D-02 -7.88508639D-05
  5.12522379D-08 -1.37033846D-11  0.00000000D+00 -6.17623606D+03  1.09334094D+02
   1000.000  6000.000 7 -2.0 -1.0  0.0  1.0  2.0  3.0  4.0  0.0        10518.689
  3.40872512D+06 -1.37483642D+04  2.36588483D+01 -2.42372856D-03  4.43116915D-07
 -4.35234840D-11  1.77521829D-15  0.00000000D+00  8.82035634D+04 -1.37126834D+02
Heat of Formation at 0 deg K    61002.72
CH4               Gurvich,1991 pt1 p44 pt2 p36. NJG added 11-4-10
 2 g 8/99 C   1.00H   4.00    0.00    0.00    0.00 0     16.04246     -74600.000
    200.000  1000.000 7 -2.0 -1.0  0.0  1.0  2.0  3.0  4.0  0.0        10016.202
 -1.76685099D+05  2.78618102D+03 -1.20257785D+01  3.91761929D-02 -3.61905443D-05
  2.02685304D-08 -4.97670549D-12  0.00000000D+00 -2.33131436D+04  8.90432275D+01
   1000.000  6000.000 7 -2.0 -1.0  0.0  1.0  2.0  3.0  4.0  0.0        10016.202
  3.73004276D+06 -1.38350148D+04  2.04910709D+01 -1.96197475D-03  4.72731304D-07
 -3.72881469D-11  1.62373720D-15  0.00000000D+00  7.53206691D+04 -1.21912488D+02
Heat of Formation at 0 deg K    -66600.0
O                 D0(O2):Brix,1954. Moore,1976. Gordon,1999.
 3 g 5/97 O   1.00    0.00    0.00    0.00    0.00 0   15.9994000     249175.003
    200.000   1000.0007 -2.0 -1.0  0.0  1.0  2.0  3.0  4.0  0.0         6725.403
-7.953611300D+03 1.607177787D+02 1.966226438D+00 1.013670310D-03-1.110415423D-06
 6.517507500D-10-1.584779251D-13 0.000000000D+00 2.840362437D+04 8.404241820D+00
   1000.000   6000.0007 -2.0 -1.0  0.0  1.0  2.0  3.0  4.0  0.0         6725.403
 2.619020262D+05-7.298722030D+02 3.317177270D+00-4.281334360D-04 1.036104594D-07
-9.438304330D-12 2.725038297D-16 0.000000000D+00 3.392428060D+04-6.679585350D-01
   6000.000  20000.0007 -2.0 -1.0  0.0  1.0  2.0  3.0  4.0  0.0         6725.403
 1.779004264D+08-1.082328257D+05 2.810778365D+01-2.975232262D-03 1.854997534D-07
-5.796231540D-12 7.191720164D-17 0.000000000D+00 8.890942630D+05-2.181728151D+02
Heat of Formation at 0 deg K    246790.000
O2                Oxygen. Gurvich et al. v1, pt 2, p9, 1989.
 3 tpis89 O   2.00    0.00    0.00    0.00    0.00 0     31.99880          0.000
```

```
   200.000  1000.000 7 -2.0 -1.0  0.0  1.0  2.0  3.0  4.0  0.0         8680.104
-3.42556269D+04  4.84699986D+02  1.11901159D+00  4.29388743D-03 -6.83627313D-07
-2.02337478D-09  1.03904064D-12  0.00000000D+00 -3.39145434D+03  1.84969912D+01
  1000.000  6000.000 7 -2.0 -1.0  0.0  1.0  2.0  3.0  4.0  0.0         8680.104
-1.03793994D+06  2.34483275D+03  1.81972949D+00  1.26784887D-03 -2.18807142D-07
 2.05372411D-11 -8.19349062D-16  0.00000000D+00 -1.68901253D+04  1.73871835D+01
  6000.000 20000.000 7 -2.0 -1.0  0.0  1.0  2.0  3.0  4.0  0.0         8680.104
 4.97515261D+08 -2.86602339D+05  6.69015464D+01 -6.16971869D-03  3.01623757D-07
-7.42087888D-12  7.27744063D-17  0.00000000D+00  2.29348755D+06 -5.53044968D+02
Heat of Formation at 0 deg K    0.0
CO                Props & Hf298: TPIS vo2,pt2,1979,p29.
 3 tpis79 C   1.00O   1.00    0.00    0.00    0.00 0     28.01040    -110530.000
   200.000  1000.000 7 -2.0 -1.0  0.0  1.0  2.0  3.0  4.0  0.0         8671.000
 1.48902756D+04 -2.92225101D+02  5.72445844D+00 -8.17613703D-03  1.45688600D-05
-1.08773326D-08  3.02790552D-12  0.00000000D+00 -1.30306969D+04 -7.85914734D+00
  1000.000  6000.000 7 -2.0 -1.0  0.0  1.0  2.0  3.0  4.0  0.0         8671.000
 4.61913571D+05 -1.94467998D+03  5.91664165D+00 -5.66420842D-04  1.39879619D-07
-1.78765700D-11  9.62081083D-16  0.00000000D+00 -2.46577624D+03 -1.38739540D+01
  6000.000 20000.000 7 -2.0 -1.0  0.0  1.0  2.0  3.0  4.0  0.0         8671.000
 8.86856197D+08 -7.50029052D+05  2.49544563D+02 -3.95630431D-02  3.29773292D-06
-1.31839424D-10  1.99891413D-15  0.00000000D+00  5.70135535D+06 -2.06068058D+03
Heat of Formation at 0 deg K    -113810.
CO2               Props & Hf298: TPIS v2,pt1,1991,p27.
 3 l 7/88 C   1.00O   2.00    0.00    0.00    0.00 0     44.00980    -393510.000
   200.000  1000.000 7 -2.0 -1.0  0.0  1.0  2.0  3.0  4.0  0.0         9365.469
 4.94378364D+04 -6.26429208D+02  5.30181336D+00  2.50360057D-03 -2.12470010D-07
-7.69148680D-10  2.84997991D-13  0.00000000D+00 -4.52818986D+04 -7.04876965D+00
  1000.000  6000.000 7 -2.0 -1.0  0.0  1.0  2.0  3.0  4.0  0.0         9365.469
 1.17696943D+05 -1.78880147D+03  8.29154353D+00 -9.22477831D-05  4.86963541D-09
-1.89206384D-12  6.33067509D-16  0.00000000D+00 -3.90834501D+04 -2.65268192D+01
  6000.000 20000.000 7 -2.0 -1.0  0.0  1.0  2.0  3.0  4.0  0.0         9365.469
-1.54440594D+09  1.01683595D+06 -2.56137666D+02  3.36936340D-02 -2.18115756D-06
 6.99132366D-11 -8.84221052D-16  0.00000000D+00 -8.04312703D+06  2.25415288D+03
Heat of Formation at 0 deg K    -393149.56
H                 D0(H2):Herzberg,1970. Moore,1972. Gordon,1999.
 3 g 6/97 H   1.00    0.00    0.00    0.00    0.00 0    1.0079400     217998.828
   200.000   1000.0007 -2.0 -1.0  0.0  1.0  2.0  3.0  4.0  0.0         6197.428
 0.000000000D+00 0.000000000D+00 2.500000000D+00 0.000000000D+00 0.000000000D+00
 0.000000000D+00 0.000000000D+00 0.000000000D+00 2.547370801D+04-4.466828530D-01
  1000.000   6000.0007 -2.0 -1.0  0.0  1.0  2.0  3.0  4.0  0.0         6197.428
```

```
 6.078774250D+01-1.819354417D-01 2.500211817D+00-1.226512864D-07 3.732876330D-11
-5.687744560D-15 3.410210197D-19 0.000000000D+00 2.547486398D+04-4.481917770D-01
   6000.000  20000.0007 -2.0 -1.0  0.0  1.0  2.0  3.0  4.0  0.0         6197.428
 2.173757694D+08-1.312035403D+05 3.399174200D+01-3.813999680D-03 2.432854837D-07
-7.694275540D-12 9.644105630D-17 0.000000000D+00 1.067638086D+06-2.742301051D+02
Heat of Formation at 0 deg K    216035.000
H2               Hydrogen. GLUSHKO ET.AL. v1, pt2, 1978, pp31-32.
 3 tpis78 H   2.00    0.00    0.00    0.00    0.00 0      2.01588          0.000
    200.000  1000.000 7 -2.0 -1.0  0.0  1.0  2.0  3.0  4.0  0.0         8468.102
  4.07832281D+04 -8.00918545D+02  8.21470167D+00 -1.26971436D-02  1.75360493D-05
 -1.20286016D-08  3.36809316D-12  0.00000000D+00  2.68248438D+03 -3.04378866D+01
   1000.000  6000.000 7 -2.0 -1.0  0.0  1.0  2.0  3.0  4.0  0.0         8468.102
  5.60812338D+05 -8.37149134D+02  2.97536304D+00  1.25224993D-03 -3.74071842D-07
  5.93662825D-11 -3.60699573D-15  0.00000000D+00  5.33981585D+03 -2.20276405D+00
   6000.000 20000.000 7 -2.0 -1.0  0.0  1.0  2.0  3.0  4.0  0.0         8468.102
  4.96671613D+08 -3.14744812D+05  7.98388750D+01 -8.41450419D-03  4.75306044D-07
 -1.37180973D-11  1.60537460D-16  0.00000000D+00  2.48835466D+06 -6.69552419D+02
Heat of Formation at 0 deg K    0.0
OH               D0(H-OH): Ruscic,2002. Gurvich,1978 pt1 p110 pt2 p37.
 3 g 4/02 O   1.00H   1.00    0.00    0.00    0.00 0   17.0073400      37278.206
    200.000  1000.000 7 -2.0 -1.0  0.0  1.0  2.0  3.0  4.0  0.0         8813.106
-1.998858990D+03 9.300136160D+01 3.050854229D+00 1.529529288D-03-3.157890998D-06
 3.315446180D-09-1.138762683D-12 0.000000000D+00 2.991214235D+03 4.674110790D+00
   1000.000  6000.000 7 -2.0 -1.0  0.0  1.0  2.0  3.0  4.0  0.0         8813.106
 1.017393379D+06-2.509957276D+03 5.116547860D+00 1.305299930D-04-8.284322260D-08
 2.006475941D-11-1.556993656D-15 0.000000000D+00 2.019640206D+04-1.101282337D+01
   6000.000 20000.000 7 -2.0 -1.0  0.0  1.0  2.0  3.0  4.0  0.0         8813.106
 2.847234193D+08-1.859532612D+05 5.008240900D+01-5.142374980D-03 2.875536589D-07
-8.228817960D-12 9.567229020D-17 0.000000000D+00 1.468393908D+06-4.023555580D+02
Heat of Formation at 0 deg K    38390.000
H2O              CODATA,1989. JRNBS v92,1987,p35. TRC tuv-25,10/88.
 2 l 8/89 H   2.00O   1.00    0.00    0.00    0.00 0     18.01528    -241826.000
    200.000  1000.000 7 -2.0 -1.0  0.0  1.0  2.0  3.0  4.0  0.0         9904.092
 -3.94795999D+04  5.75572977D+02  9.31783351D-01  7.22271091D-03 -7.34255448D-06
  4.95504134D-09 -1.33693261D-12  0.00000000D+00 -3.30397425D+04  1.72420539D+01
   1000.000  6000.000 7 -2.0 -1.0  0.0  1.0  2.0  3.0  4.0  0.0         9904.092
  1.03497224D+06 -2.41269895D+03  4.64611114D+00  2.29199814D-03 -6.83683007D-07
  9.42646842D-11 -4.82238028D-15  0.00000000D+00 -1.38428625D+04 -7.97815119D+00
Heat of Formation at 0 deg K    -238918.95
HO2              Hf:Hills,1984 & NASA data. Jacox,1998 p153.
```

```
 2 g 4/02 H   1.00O   2.00    0.00    0.00    0.00 0   33.0067400      12020.000
    200.000  1000.000 7 -2.0 -1.0  0.0  1.0  2.0  3.0  4.0  0.0        10002.162
-7.598882540D+04 1.329383918D+03-4.677388240D+00 2.508308202D-02-3.006551588D-05
 1.895600056D-08-4.828567390D-12 0.000000000D+00-5.873350960D+03 5.193602140D+01
   1000.000  6000.000 7 -2.0 -1.0  0.0  1.0  2.0  3.0  4.0  0.0        10002.162
-1.810669724D+06 4.963192030D+03-1.039498992D+00 4.560148530D-03-1.061859447D-06
 1.144567878D-10-4.763064160D-15 0.000000000D+00-3.200817190D+04 4.066850920D+01
Heat of Formation at 0 deg K    12020.000
H2O2              Hf:Gurvich,1989 pt1 p127. Gurvich,1978 pt1 p121.
 2 g 6/99 H   2.00O   2.00    0.00    0.00    0.00 0   34.0146800    -135880.000
    200.000   1000.0007 -2.0 -1.0  0.0  1.0  2.0  3.0  4.0  0.0        11158.835
-9.279533580D+04 1.564748385D+03-5.976460140D+00 3.270744520D-02-3.932193260D-05
 2.509255235D-08-6.465045290D-12 0.000000000D+00-2.494004728D+04 5.877174180D+01
   1000.000   6000.0007 -2.0 -1.0  0.0  1.0  2.0  3.0  4.0  0.0        11158.835
 1.489428027D+06-5.170821780D+03 1.128204970D+01-8.042397790D-05-1.818383769D-08
 6.947265590D-12-4.827831900D-16 0.000000000D+00 1.418251038D+04-4.650855660D+01
Heat of Formation at 0 deg K    -135880.000
N2                Nitrogen. GLUSHKO ET.AL. v1, pt2, p207, 1978.
 3 tpis78 N   2.00    0.00    0.00    0.00    0.00 0     28.01348          0.000
    200.000  1000.000 7 -2.0 -1.0  0.0  1.0  2.0  3.0  4.0  0.0         8670.104
  2.21037122D+04 -3.81846145D+02  6.08273815D+00 -8.53091381D-03  1.38464610D-05
 -9.62579293D-09  2.51970560D-12  0.00000000D+00  7.10845911D+02 -1.07600320D+01
   1000.000  6000.000 7 -2.0 -1.0  0.0  1.0  2.0  3.0  4.0  0.0         8670.104
  5.87709908D+05 -2.23924255D+03  6.06694267D+00 -6.13965296D-04  1.49179819D-07
 -1.92309442D-11  1.06194871D-15  0.00000000D+00  1.28320618D+04 -1.58663484D+01
   6000.000 20000.000 7 -2.0 -1.0  0.0  1.0  2.0  3.0  4.0  0.0         8670.104
  8.30971200D+08 -6.42048187D+05  2.02020507D+02 -3.06501961D-02  2.48685558D-06
 -9.70579208D-11  1.43751673D-15  0.00000000D+00  4.93850663D+06 -1.67204791D+03
Heat of Formation at 0 deg K    0.0
FINITE RATE COEFFICIENTS
 REF: BAURLE AIAA JPP, Vol. 18, No. 5, pp. 990-1002, FROM MAWID

    23,7      NREQ,NDEQ
   300.      TFRMIN
H    1. O2   1. HO2   1.           0.0      -505.05       1.5E+15
                                   0.0       0.0          0.0
third body efficiency  0
OH   1. OH   1. H2O2  1.           0.0       0.0          0.0
                                   0.0       2.298E+4     1.2E+17
third body efficiency  0
```

```
CO   1. O    1. CO2   1.          0.0       0.207E+4     5.9E+15
                                  0.0       0.0          0.0
third body efficiency  0
O    1. H    1. OH    1.          0.0       0.0          0.0
                                 -1.0       5.237E+4     8.0E+19
third body efficiency  0
O    1. O    1. O2    1.          0.0       0.0          0.0
                                  0.0       5.808E+4     5.1E+15
third body efficiency  0
H    1. H    1. H2    1.          0.0       0.0          0.0
                                  0.0       4.848E+4     2.2E+14
third body efficiency  0
H    1. OH   1. H2O   1.          0.0       0.0          0.0
                                  0.0       5.303E+4     2.2E+16
third body efficiency  0
H    1. O2   1. O    1. OH   1.   0.0       0.8484E+04   2.20E+14
                                  0.0       0.0          0.0
H2   1. O    1. H    1. OH   1.   1.0       0.4495E+04   1.80E+10
                                  0.0       0.0          0.0
O    1. H2O  1. OH   1. OH   1.   0.0       0.9293E+04   6.80E+13
                                  0.0       0.0          0.0
OH   1. H2   1. H    1. H2O  1.   0.0       0.2576E+04   2.20E+13
                                  0.0       0.0          0.0
O    1. HO2  1. O2   1. OH   1.   0.0       0.0505E+04   5.00E+13
                                  0.0       0.0          0.0
H    1. HO2  1. OH   1. OH   1.   0.0       0.9596E+03   2.50E+14
                                  0.0       0.0          0.0
H    1. HO2  1. H2   1. O2   1.   0.0       0.3535E+03   2.50E+13
                                  0.0       0.0          0.0
OH   1. HO2  1. H2O  1. O2   1.   0.0       0.5051E+03   5.00E+13
                                  0.0       0.0          0.0
HO2  1. HO2  1. H2O2 1. O2   1.   0.0       0.5051E+03   1.00E+13
                                  0.0       0.0          0.0
HO2  1. H2   1. H2O2 1. H    1.   0.0       0.9444E+04   7.30E+11
                                  0.0       0.0          0.0
H2O2 1. OH   1. H2O  1. HO2  1.   0.0       0.9091E+03   1.00E+13
                                  0.0       0.0          0.0
CO   1. OH   1. CO2  1. H    1.   1.3      -0.4040E+03   1.50E+7
                                  0.0       0.0          0.0
CO   1. O2   1. CO2  1. O    1.   0.0       1.8990E+04   3.10E+11
```

```
                                    0.0       0.0          0.0
CO   1. HO2  1. CO2  1. OH   1.     0.0       1.1970E+04   1.50E+14
                                    0.0       0.0          0.0
GLOBAL
1.   C2H4      1.   O2                        2.   CO        2.   H2
 0.0       1.5098E+04   4.30E+12
 EXPONENTS
  0.10 1.65 0.   0.   0.   0.
GLOBAL
1.   CH4       0.5  O2                        1.   CO        2.   H2
 0.0       1.5098E+04   2.30E+7
 EXPONENTS
 -0.30 1.30 0.   0.   0.   0.
TRANSPORT COEFFICIENTS
C2H4          1   300.000   8000.00   5.6640E-01  5.4000E+03  5.9655E+02
                                      2.0104E-01  5.4000E+03  2.6625E+03
CH4           1   300.000   8000.00   1.0309E-01  4.9160E+02  3.7971E+02
                                      1.7697E-02  4.9160E+02  4.5387E+03
O             1   300.000  8000.000   1.7430E-01  4.9160E+02  2.8260E+02
                                      1.0360E-02  4.9160E+02  2.3500E+02
O2            1   300.000   8000.00   1.9190E-01  4.9160E+02  2.5000E+02
                                      1.4190E-02  4.9160E+02  4.0000E+02
CO            1   300.000   8000.00   1.6570E-01  4.9160E+02  2.4500E+02
                                      1.3420E-02  4.9160E+02  3.2000E+02
CO2           1   300.000   8000.00   1.3700E-01  4.9160E+02  4.0000E+02
                                      8.4070E-03  4.9160E+02  4.0000E+03
H             1   300.000  8000.000   7.0060E-02  4.9160E+02  2.1180E+02
                                      1.2530E-01  4.9160E+02  2.1207E+02
H2            1   300.000   8000.00   8.4110E-02  4.9160E+02  1.7400E+02
                                      9.4000E-02  4.9160E+02  3.0000E+02
OH            1   300.000  8000.000   1.8260E-01  4.9160E+02  2.4966E+02
                                      2.6180E-02  4.9160E+02  4.1541E+02
H2O           1   300.000   8000.00   1.7030E-01  7.5000E+02  1.5500E+03
                                      1.0360E-02  4.9160E+02  2.3000E+03
HO2           1   300.000  8000.000   1.7030E-01  7.5000E+02  1.5500E+03
                                      1.0360E-02  4.9160E+02  2.3000E+03
H2O2          1   300.000  8000.000   1.7030E-01  7.5000E+02  1.5500E+03
                                      1.0360E-02  4.9160E+02  2.3000E+03
N2            1   300.000   8000.00   1.6630E-01  4.9160E+02  1.9200E+02
                                      1.4000E-02  4.9160E+02  3.0000E+02
```